Neuron

Article

Extrinsic control and intrinsic computation in the hippocampal CA1 circuit

Graphical abstract

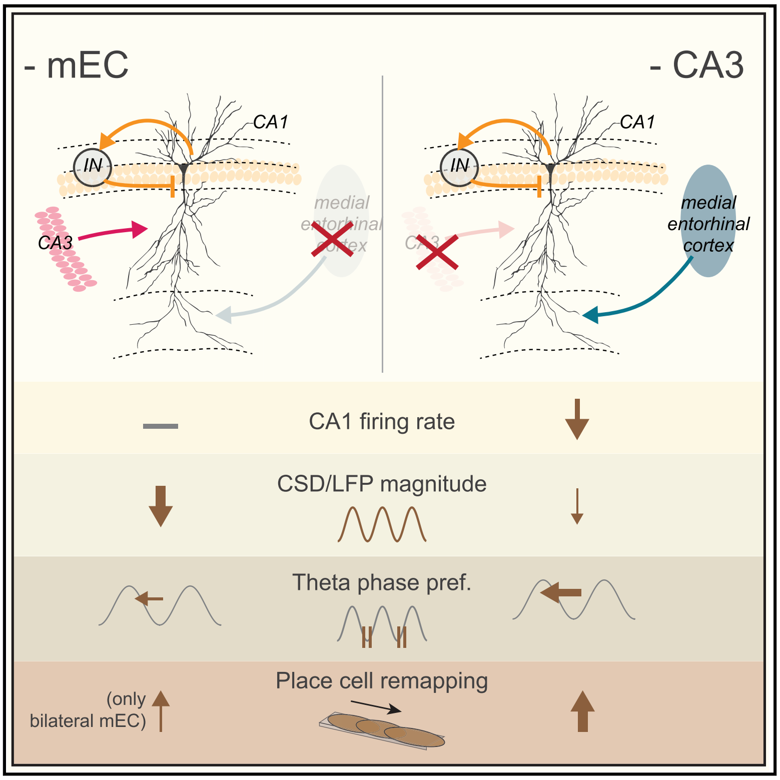
- mEC
- CA3
CA1
IN
CA3
medial entorhinal cortex
CA1
IN
CA3
medial entorhinal cortex
CA1 firing rate
CSD/LFP magnitude
Theta phase pref.
Place cell remapping
(only bilateral mEC)

Highlights

- Unilateral or bilateral silencing of the mEC decreases theta and gamma currents
- Bilateral but not unilateral mEC silencing causes remapping in CA1 cell assemblies
- CA3 silencing decreases CA1 firing rates and leads to place cell remapping
- CA1 place cells and assemblies persist despite combined mEC and CA3 silencing

Authors

Ipshita Zutshi, Manuel Valero,
Antonio Fernández-Ruiz,
György Buzsáki

Correspondence

gyorgy.buzsaki@nyumc.org

In brief

Zutshi et al. perform simultaneous silencing of major afferents into the hippocampal CA1 to address whether CA1 spiking can be sustained by local computations. These manipulations reveal that coordinated CA1 place cell assemblies persist with minimal input but that each input has distinct effects on spatial tuning and field potentials.

Zutshi et al., 2022, Neuron *110*, 1–16
February 16, 2022 © 2021 Elsevier Inc.
https://doi.org/10.1016/j.neuron.2021.11.015

CellPress

Please cite this article in press as: Zutshi et al., Extrinsic control and intrinsic computation in the hippocampal CA1 circuit, Neuron (2021), https://doi.org/10.1016/j.neuron.2021.11.015

Neuron

CellPress

Article

Extrinsic control and intrinsic computation in the hippocampal CA1 circuit

Ipshita Zutshi,[1] Manuel Valero,[1] Antonio Fernández-Ruiz,[1,3] and György Buzsáki[1,2,4,*]
[1]New York University Neuroscience Institute, New York University, New York, NY 10016, USA
[2]Center for Neural Science, New York University, New York, NY 10016, USA
[3]Present address: Department of Neurobiology and Behavior, Cornell University, Ithaca, NY 14850, USA
[4]Lead contact
*Correspondence: gyorgy.buzsaki@nyumc.org

https://doi.org/10.1016/j.neuron.2021.11.015

SUMMARY

In understanding circuit operations, a key problem is the extent to which neuronal spiking reflects local computation or responses to upstream inputs. We addressed this issue in the hippocampus by performing combined optogenetic and pharmacogenetic local and upstream inactivation. Silencing the medial entorhinal cortex (mEC) largely abolished extracellular theta and gamma currents in CA1 while only moderately affecting firing rates. In contrast, CA3 and local CA1 silencing strongly decreased firing of CA1 neurons without affecting theta currents. Each perturbation reconfigured the CA1 spatial map. However, the ability of the CA1 circuit to support place field activity persisted, maintaining the same fraction of spatially tuned place fields and reliable assembly expression as in the intact mouse. Thus, the CA1 network can induce and maintain coordinated cell assemblies with minimal reliance on its inputs, but these inputs can effectively reconfigure and assist in maintaining stability of the CA1 map.

INTRODUCTION

In contrast to the modularly organized neocortex, the vast majority of synaptic connections in the hippocampus are supplied from its own neurons, most notably by the extensive collaterals of the CA3 pyramidal neurons (Witter, 2007). Its most important extrinsic afferents arrive from the entorhinal cortex and other retrohippocampal and thalamic structures, supplemented by subcortical inputs (Amaral and Lavenex, 2007). The entorhinal inputs provide communication with the rest of the neocortex and the outside world, whereas the subcortical neuromodulators toggle the hippocampal physiological dynamic between two fundamental computational modes: an interactive mode, characterized by theta oscillations (5–9 Hz), and an intrinsic, self-organized sharp wave ripple mode. Interfering with theta oscillations, typically brought about by manipulating the septal "pacemaker," results in behavioral impairments comparable with surgical damage of the hippocampus (Winson, 1978). During explorative behavior and learning, theta oscillations organize the temporal structure of neurons, as amply illustrated by the relationship between the spatial position of the animal and the phase of the theta waves at which place cells spike ("phase precession"; O'Keefe and Recce, 1993) and by the relationship between the distances of place fields and the theta phase offsets of place field spikes (Dragoi and Buzsáki, 2006). Several previous studies have been devoted to understanding the relationship between behavior on one hand and the contribution of mesoscopic theta waves and the spiking activity of neurons on the other. A key question that remains is to what extent hippocampal neuronal activity reflects intrinsic local computation as opposed to "inheritance" from upstream inputs (Mizuseki et al., 2009). This is a particularly relevant question in the CA1 region, in which connections between the pyramidal neurons are very sparse (Amaral and Lavenex, 2007; Bezaire and Soltesz, 2013; Deuchars and Thomson, 1996).

Early studies used lesions and pharmacological inactivation of various structures to evaluate the relative contribution of the intrinsic versus extrinsic afferents on physiology and behavior. Damaging CA3 neurons (Brun et al., 2002) or their chemogenetic silencing (Keinath et al., 2020) or suppressing their spiking by inhibiting the septum yielded only minor changes in CA1 place responses (Mizumori et al., 1989). Selectively blocking vesicle release at CA3 terminals by a molecular approach did not affect firing rates but altered place field sizes (Middleton and McHugh, 2016; Nakashiba et al., 2008, 2009). In contrast, local optogenetic silencing of CA3-to-CA1 afferents decreased the firing rate and spatial properties of CA1 place cells (Davoudi and Foster, 2019). However, in a similar optogenetic silencing study, an increase in CA1 firing rates was reported, accompanied by a decrease in theta-modulated slow gamma oscillation (El-Gaby et al., 2021).

The discovery of grid cells in the medial entorhinal cortex (mEC; Hafting et al., 2005) boosted investigation of the effect of the mEC on hippocampal physiology. Large lesions of the entorhinal cortex, including the medial and lateral parts, reduced

Please cite this article in press as: Zutshi et al., Extrinsic control and intrinsic computation in the hippocampal CA1 circuit, Neuron (2021), https://doi.org/10.1016/j.neuron.2021.11.015

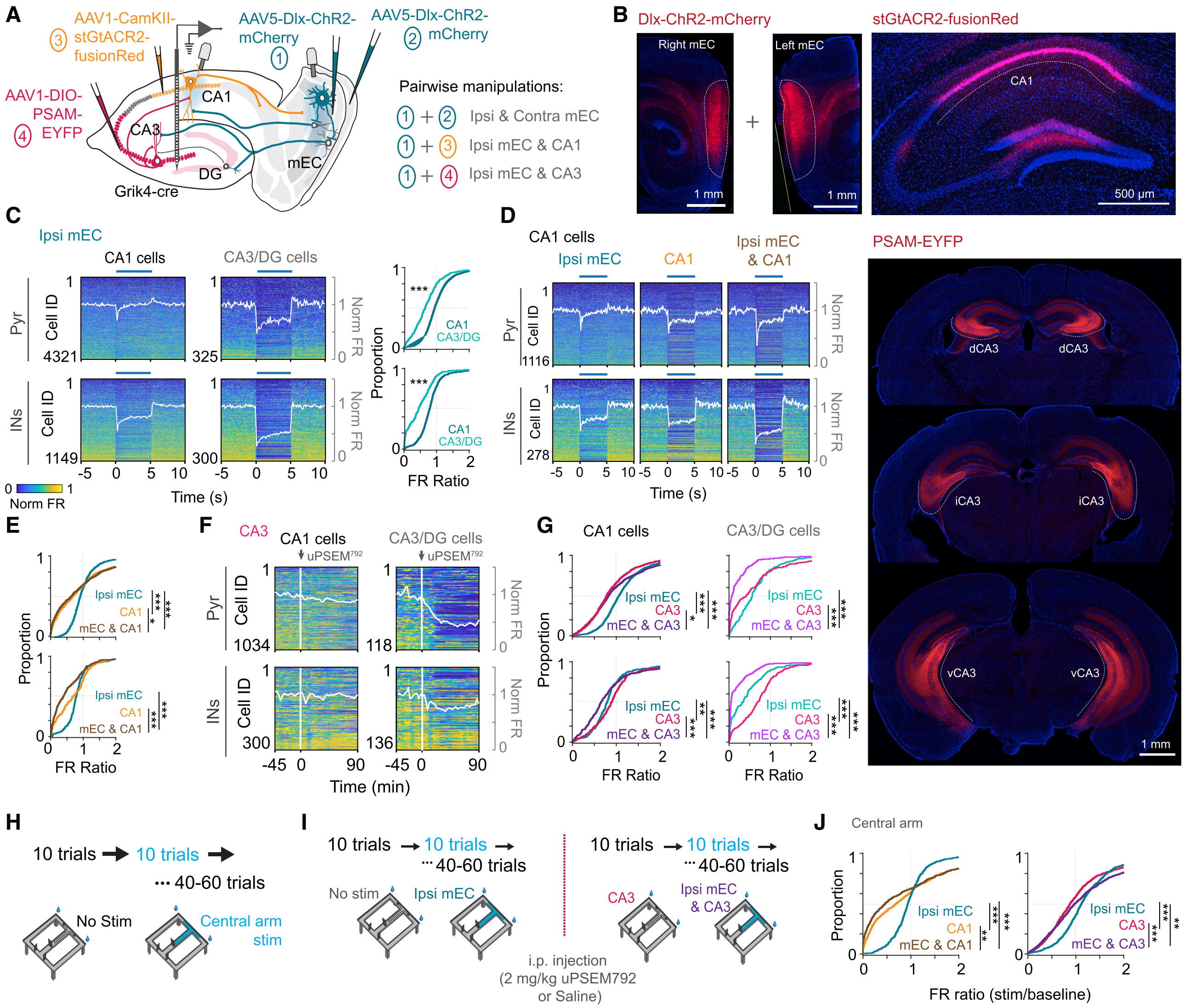

Figure 1. Transient functional deafferentation of CA1 region by optogenetic and pharmacogenetic manipulations

(A) Schematic of the approach used for pairwise silencing of mEC, CA3, and local CA1 pyramidal cells. AAV-Dlx-ChR2 was injected bilaterally or unilaterally into the mEC to express ChR2 in all inhibitory interneuron types, and optic fibers were implanted bilaterally or unilaterally over the mEC. For CA3 silencing, AAV-DIO-PSAM was injected bilaterally along the entire dorsoventral CA3 axis of Grik4-cre mice, which express Cre in CA3 and DG neurons. For local CA1 inhibition, AAV-CaMKII-stGtACR2 was injected unilaterally into CA1, and an optic fiber was implanted over CA1. A single- or multiple-shank silicone probe was implanted into the hippocampus.

(B) Representative histology for each of the described manipulations. Left: sagittal sections showing virus expression labeling interneurons with ChR2 across all layers of the mEC. Right: coronal section showing spread of stGtACR2 largely restricted to CA1. Bottom: coronal sections with bilateral expression of PSAM along the entire extent of CA3.

(C) Left: firing rate changes of pyramidal cells and putative interneurons in CA1 and CA3/DG regions in response to 5-s-long optogenetic inhibition of the ipsilateral mEC in the home cage (blue bar). Each row of the heatmap is a cell normalized by its peak firing rate. White trace, average population firing rate. Right: CDF plots comparing the firing rate ratio between stimulation and baseline epochs for CA1 and CA3/DG pyramidal cells (top, Wilcoxon rank-sum test, $Z = 12.92$, $p < 0.001$) and interneurons (bottom, Wilcoxon rank-sum test, $Z = 12.27$, $p < 0.001$).

(D) Plots as described in (C) but for cells recorded from CA1 in response to ipsilateral mEC, CA1, and combined ipsi mEC and CA1 silencing.

(E) CDF plots showing effective inhibition of pyramidal cells by the CA1 manipulation (top, Friedman test followed by Tukey-Kramer post hoc tests, chi-square(2,2236) = 96.79, $p < 0.001$) and interneurons by combined ipsilateral (ipsi) mEC and CA1 silencing (bottom, chi-square(2,554) = 88.46, $p < 0.001$).

(F) Firing rate responses of CA1 and CA3/DG pyramidal cells and interneurons before and after injection of μPSEM^{792}. White trace, average population firing rate.

(G) Cumulative density function plots showing the firing rate changes after ipsi mEC, CA3, and combined ipsi mEC and CA3 silencing for CA1 and CA3/DG pyramidal cells (Friedman test followed by Tukey-Kramer post hoc tests; CA1: top left, chi-square(2,2146) = 152.73, $p < 0.001$; CA3/DG: top right, chi-square(2,306) = 155.77, $p < 0.001$) and interneurons (CA1: bottom left, chi-square(2,604) = 63.29, $p < 0.001$; CA3/DG: bottom right, chi-square(2,348) = 139.70, $p < 0.001$).

(legend continued on next page)

Please cite this article in press as: Zutshi et al., Extrinsic control and intrinsic computation in the hippocampal CA1 circuit, Neuron (2021), https://doi.org/10.1016/j.neuron.2021.11.015

theta/gamma oscillations (Bragin et al., 1995; Kamondi et al., 1998; Ormond and McNaughton, 2015; Schlesiger et al., 2015), decreased the fraction of hippocampal CA1 place cells, and affected various features of place field properties (Brun et al., 2008; Chenani et al., 2019; Hales et al., 2014; Miller and Best, 1980; Ormond and McNaughton, 2015; Sabariego et al., 2019; Schlesiger et al., 2015, 2018). More recent studies used optogenetic and pharmacogenetic techniques to readdress the role of the entorhinal inputs on hippocampal circuits. Optogenetic suppression of entorhinal inputs by directly suppressing the spiking activity of superficial layer neurons or activating the inhibitory neuronal population affected the temporal properties of neuronal spiking and induced partial or major remapping of place representation in the hippocampus, although often without major disruption of the spatial firing properties of individual neurons (Fernández-Ruiz et al., 2021; Miao et al., 2015; Rueckemann et al., 2016), leading to the suggestion that the mEC is responsible for remapping of hippocampal place cells (Latuske et al., 2018; Miao et al., 2015; but see Schlesiger et al., 2018). In contrast, another study (Robinson et al., 2017) reported that mEC inactivation produced a deficit in temporal coding in CA1 neurons, associated with impairment in memory across a temporal delay, whereas spatial and object coding remained intact. Spike suppression of mEC neurons by pharmacogenetic perturbation induced remapping in CA3 (Miao et al., 2015). Relatively selective excitation, but not inhibition, of layer 2 mEC neurons by pharmacogenetic means was sufficient to induce partial remapping and affect the spatial firing correlates of CA1 pyramidal neurons (Kanter et al., 2017).

Despite the intense and careful work in this research area, the magnitudes and types of the reported physiological and spatial correlation impairments, and the interpretations of the mechanisms of the experimental interventions vary widely across experiments. At least part of the existing variability and conflicts is due to the different behavioral paradigms, designs, and evaluation methods used by different investigators. Simultaneous manipulations in the same animal or even separate manipulations of the different inputs to the hippocampal circuits in the same experiment are rare (Fernández-Ruiz et al., 2021). Most studies focusing on spiking activity of neurons used recordings from the cell body layers, precluding evaluation of layer-specific effects of the applied perturbations. Conversely, experiments dedicated to studying mesoscopic network effects lacked single-neuron resolution to address the importance of neuron-circuit interactions. Therefore, the goals of our experiments were to examine and compare the contribution of local hippocampal circuits and major inputs on the temporal organization of neurons at the mesoscopic and microscopic scales by selective targeted perturbations and to relate the observed network changes to the ensuing spatial ''representations'' (inheritance versus local induction) of CA1 hippocampal neurons. Each manipulation was performed in the same hippocampus-dependent spatial alternation paradigm (Ainge et al., 2007) and during rest/sleep, allowing head-to-head comparison of the consequences of separate and combined interventions. To achieve these goals, we used combinations of optogenetic silencing of the unilateral and bilateral mEC and local CA1 region and bilateral pharmacogenetic silencing of the entire CA3 region, combined with high spatial resolution recording of local field potentials (LFP) in the CA1-dentate axis and simultaneously collecting firing pattern data from thousands of single neurons. Our study revealed a much higher input-independent computation in the CA1 region than predicted by previous studies.

RESULTS

Transient functional deafferentation of the hippocampus

To quantitatively assess the physiological contribution of the various inputs to the CA1 circuit, we used a combination of optogenetic and pharmacogenetic manipulations. These transient manipulations (''functional deafferentation'') allowed us to compare the effect of specific inputs on LFP and spiking of the same neuronal populations within the same animal and session. To silence the mEC, we infected all types of GABAergic interneurons by AAV5-mDlx-ChR2-mCherry virus in one or both hemispheres (n = 18 and n = 3 mice, respectively; Figure 1A). The virus evenly infected large populations of interneurons throughout the dorsal and midparts of the superficial layers of the mEC as well as interneurons within the deep layers (Figures 1B and S1A; Fernández-Ruiz et al., 2021). To address the contribution of local circuit computations, CA1 pyramidal neurons were infected with a virus expressing the inhibitory opsin stGtACR2-fusionRed (Mahn et al., 2018) under the control of a Ca^{2+}/calmodulin-dependent protein kinase II (CaMKII) promoter. The virus labeled almost the entire CA2-subicular axis of the CA1 region, confined to the dorsal hippocampus (Figures 1B and S1E–S1G), with occasional labeling of dentate gyrus (DG) neurons. Because CA3 pyramidal neurons contribute widely divergent afferents to CA1 neurons bilaterally (Li et al., 1994) and because our mEC silencing also affected the CA3/DG region, we chose bilateral pharmacogenetic suppression using a transgenic mouse line (Grik4-Cre, Cre expression in CA3/DG cells) to examine their control of the CA1 circuit. A pharmacologically selective actuator

---

(H) Recordings were also performed as the mice ran on a delayed spatial alternation task (10-s delay). Optogenetic stimulation was performed in blocks of 10 trials interleaved with 10-trial blocks of no stimulation, restricted to the central arm of the maze (region highlighted in blue).

(I) The mice used for CA3 silencing were first run on a morning session with ipsi mEC silencing on the central arm, followed by an i.p. injection of μPSEM792 or saline. They were subsequently run on a second session with ipsi mEC silencing targeted to the central arm but now with simultaneous pharmacogenetic CA3 manipulation.

(J) Left: CDF plot of firing rate ratios of CA1 pyramidal cells during CA1 and ipsi mEC manipulation in the central arm of the maze revealed similar effects as observed in the home cage (Kruskal-Wallis test followed by Tukey-Kramer post hoc tests, n[ipsi mEC, CA1, ipsi mEC and CA1] = 617, 899, 640 cells from 5 mice, chi-square(2,2153) = 77.66, $p < 0.001$). Right: CDF plot of firing rate ratios during CA3 and ipsi mEC manipulation on the central arm of the maze (Kruskal-Wallis test followed by Tukey-Kramer post hoc tests, n[ipsi mEC, CA1, ipsi mEC and CA1] = 1,082, 1,085, 1,086 cells from 6 mice, chi-square(2,3250) = 65.02, $p < 0.001$).

*$p < 0.05$, **$p < 0.01$, ***$p < 0.001$. See also Figures S1 and S2.

module (PSAM^4-GlyR) was used as a neuronal silencer, with uPSEM792 as the agonist (Magnus et al., 2019). PSAM-EYFP expression was homogeneous throughout the septotemporal axis of the CA3 region, with sparse labeling of granule cells (Figures 1B and S1E–S1G).

Before examining the effect of the various functional deafferentations on hippocampal LFPs, we assessed their effects on the firing rates of hippocampal neurons first in the home cage during rest/sleep (including periods of quiet wake and non-REM and REM sleep) and then during maze behavior. Unilateral optogenetic stimulation of inhibitory interneurons in the mEC (5-s pulses on, 25 s off) exerted a large effect on DG/CA3 neurons but, unexpectedly, only a small effect on the firing rate of the CA1 pyramidal neuron population (a stronger effect though on CA1 interneurons; Figure 1C). The magnitude of the effect on the mean population firing rate depended on the light intensity delivered to the mEC (Figure S1B). Optogenetic suppression of CA1 pyramidal neurons brought about a stronger reduction of firing rates of CA1 pyramidal cells and interneurons (Figures 1D, 1E, and S1C). As expected, PSAM^4-GlyR activation suppressed CA3 and dentate excitatory cells and dis-facilitated interneurons, and removal of the bilateral physiological excitation by CA3 neurons decreased CA1 firing rates (Figures 1F, 1G, and S1D). Combined perturbation of mEC and CA1 regions and mEC and CA3/DG regions brought about a larger decrease of CA1 neuron firing rates than the respective single-region manipulations (Figures 1E and 1G). Bilateral stimulation of the mEC also had a larger effect on firing rates than unilateral stimulation (Figure S2B). These firing rate changes were not observed in control sessions, where the mice were injected with the vehicle instead of the agonist uPSEM792 (Figure S3A).

Optogenetic stimulation during maze performance was restricted to the central arm of the maze (including a small section of the maze after the animal makes a turn) and was triggered by opening of the delay area gate and terminated by the mouse's crossing the photobeam in front of the water port (Figure 1H). Blocks of control and stimulated trials (10 trials per block) alternated until the mouse ran 50–60 trials in a session. LFP and unit firing in the (non-stimulated) side arms served as additional controls. For sessions with CA3/DG silencing, the first session with ipsilateral mEC silencing was followed by a second, identical session after intraperitoneal (i.p.) injection of the agonist or vehicle (Figure 1I). Optogenetic and pharmacogenetic manipulations on the maze induced firing rate changes qualitatively similar to those observed in the home cage (Figures 1J and S6B).

Anchoring mesoscopic patterns to anatomical landmarks

Mice were implanted with 64-site linear silicon probes (single shank or double shank) or a 5-shank probe (for many-neuron recordings; STAR Methods) in the dorsal hippocampus. The LFP traces were converted to current source density (CSD) maps to relate the domain-specific transmembrane potentials of pyramidal neurons brought about by the afferent activity to layer-specific extracellular current flow (Brankačk et al., 1993; Buzsáki et al., 1986; Fernández-Ruiz et al., 2021; Mitzdorf, 1985). The characteristic depth distribution of CSD and unit firing was used to identify three physiological patterns that reliably anchored the recording sites to CA1, CA3, and DG sublayers across animals. In unstained histological sections (Figure 2A), the distance between the mid-pyramidal layer and the hippocampal fissure along the silicon probe track was measured and related to the recording sites. The recording site with the largest-amplitude sharp wave ripple (SPW-R) marked the middle of the CA1 pyramidal layer. This site also corresponded to the largest magnitude of the sharp wave source and the largest density of discriminated spikes (Mizuseki et al., 2011; Valero et al., 2017). In turn, the sink of the sharp wave marked the middle of the *stratum* (*str.*) *radiatum*. The prominent sink during walking-related theta oscillations served as the third physiological marker and identified the *str. lacunosum moleculare* (sLM; Figure 2B; Buzsáki, 2002). An additional large theta sink, phase reversed with the one in the sLM, was used to identify the mid-molecular layer of the dentate gyrus in mice with more medial probe implantation (Figure 2A). These landmarks were highly consistent across mice, allowing group analyses (Figures S1E–S1G). Theta waves were highly coherent within and across layers and regions, with a gradual phase shift of theta waves starting below the CA1 pyramidal layer, reaching 180° in the sLM and continuing to approximately 90°/270° in the dentate hilus (Figure 2C; Brankačk et al., 1993; Buzsáki et al., 1986).

Optogenetic suppression of the entorhinal cortex reduces hippocampal theta oscillations

To maintain comparable behavioral states across manipulations, the effects of all optogenetic and pharmacogenetic silencing were tested specifically in the central arm while mice performed the memory task in the maze (Figures 2D–2K). Optogenetic pulse onset in the mEC, triggered by opening of the start area door, induced prominent current sources (representing removal of excitation) in the CA1 sLM and the mid-molecular layer of the dentate gyrus (Figure 2E). In contrast to the relatively small effect of mEC silencing on the spiking activity of CA1 pyramidal cells, theta currents, as measured during the entire stimulation period, were reduced dramatically in CA1 and the dentate gyrus (Figures 2D and 2F; Video S1), and the reduced sink maximum in the sLM shifted upward significantly (Figure S2D). The largest changes were present in the dentate molecular layer and sLM, followed by the radiatum, and a minor decrease of theta current was also observed in the CA1 pyramidal layer (Figures 2G). The magnitude of theta suppression varied with the strength of light power delivered to the mEC (Figure S1B).

Optogenetic suppression of the contralateral mEC output induced a negligible effect on the power of theta oscillations, and the effect of concurrent ipsilateral and contralateral stimulation was largely additive (Figures 2H–2K and S2G). In addition to theta, the power in the gamma frequency band was also reduced (Figures 2I and 2J). Ipsilateral but not contralateral suppression of the mEC also reduced the frequency of theta oscillations by approximately 0.5 Hz (Figure 2K), and this reduction was not due to change in running speed, which remained mostly unaffected by optogenetic stimulation (Figure S4). In addition, the theta phase coherence between the

Please cite this article in press as: Zutshi et al., Extrinsic control and intrinsic computation in the hippocampal CA1 circuit, Neuron (2021), https://doi.org/10.1016/j.neuron.2021.11.015

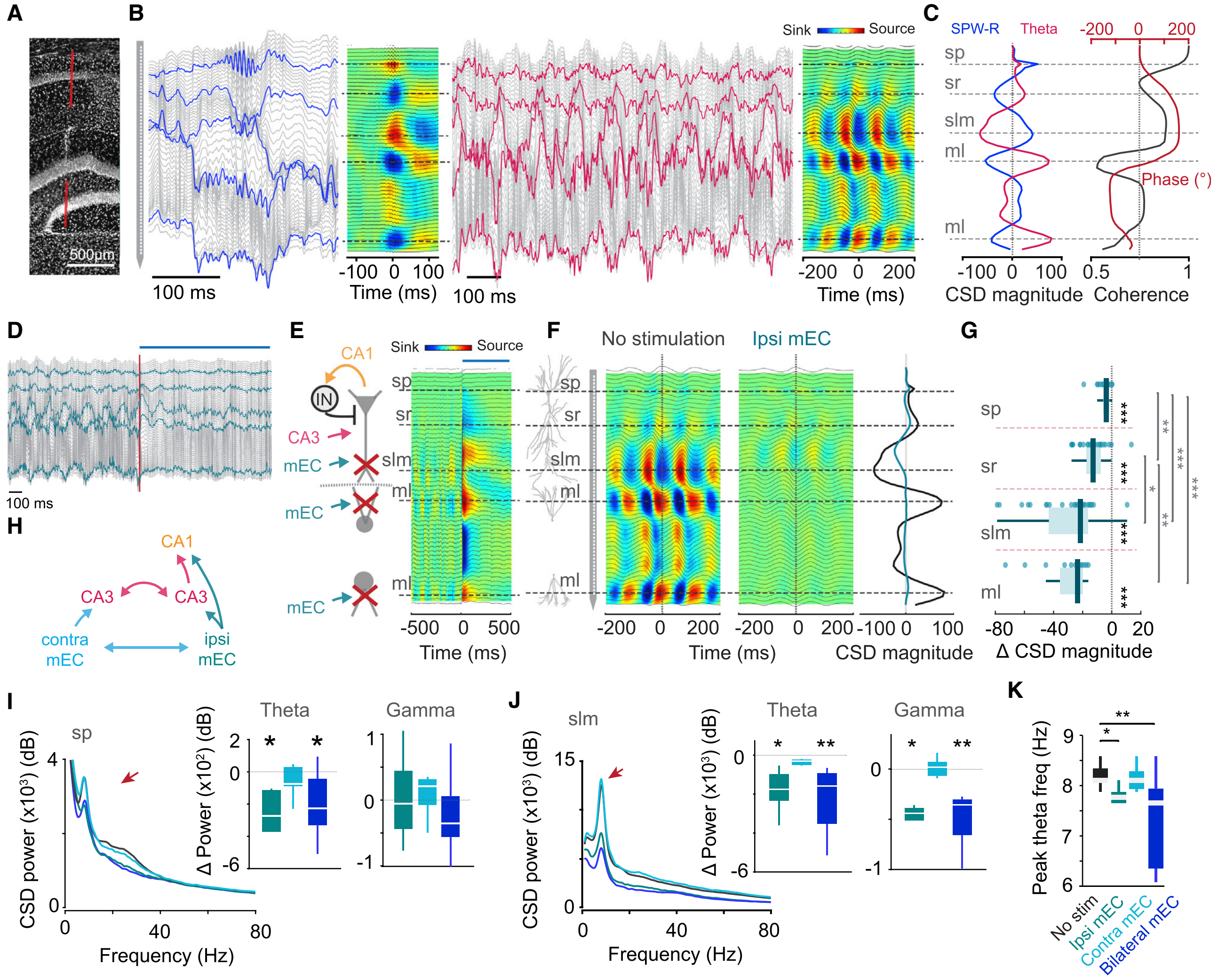

Figure 2. Ipsi mEC silencing led to a profound decrease in CA1 CSD power

(A) Track of the 64-site linear silicone probe spanning the hippocampus.

(B) LFP traces recorded across all channels. Left: example LFP traces and the resultant CSD map during a CA1 SPW-R. Horizontal dashed lines correspond to the *str. pyramidale* (sp), *str. radiatum* (sr), *str. lacunosum moleculare* (sLM), and molecular layers (mls) of the inner and outer dentate blades. Right: example theta waves and the resultant CSD map during maze running.

(C) Left trace: CSD depth profile during SPW-Rs (blue) and theta oscillations (pink) show opposing sinks and sources. Right trace: theta band coherence magnitude (black) and phase (red) of LFP as a function of depth along the CA1-DG axis.

(D) 2-s-long LFP traces during ipsi mEC silencing. The red line and blue bar indicate onset of stimulation. Blue highlighted traces indicate sp, sr, sLM, and the two ml channels, respectively.

(E) Left: schematic highlighting expected effects of mEC silencing along the CA1-DG axis. Red X, reduced inputs. Right: LFP traces (black) and CSD map in response optogenetic silencing of the ipsilateral mEC, showing prominent sources at the mEC terminal zones because of disfacilitation. The blue bar on top indicates optogenetic stimulation.

(F) Reduction of theta sinks and sources pairs along the CA1-DG axis during ipsi mEC silencing. Right: CSD plot at time zero. Black, control; blue, mEC silencing.

(G) Theta CSD magnitude decreased across all hippocampal layers, with the greatest reduction in the sLM and ml (each dot represents one session from one animal, n = 32 sessions across 13 mice; within layer: Wilcoxon signed rank test against 0, all $p < 0.001$; across layers: Kruskal-Wallis test followed by Tukey-Kramer post hoc tests, chi-square(3,105) = 56.81, $p < 0.001$).

(H) Schematic depicting potential pathways affected by contralateral versus ipsi mEC manipulation.

(I and J) Left: average power spectra of CSD across all mice upon ipsi, contralateral (contra), and bilateral mEC stimulation shows a decrease in theta and gamma CSD power in the CA1 pyramidal layer (sp; I) and sLM (J). Red arrows, theta peak. Right: change in theta (6–12 Hz) and gamma (25–90 Hz) CSD power for each manipulation compared with baseline in the sp and sLM (n[ipsi, contra, bilateral mEC] = 6, 7, and 9 sessions from 3 mice, Wilcoxon two-sided signed rank test against 0; sp: theta, p = 0.03, 0.47, 0.02, respectively; gamma, p = 1, 0.37, 0.36, respectively; sLM: theta, p = 0.03, 0.22, 0.004, respectively; gamma, p = 0.03, 0.81, 0.004, respectively). Color legend as in (H).

(K) Ipsi and bilateral but not contra mEC silencing led a decrease in theta frequency (n = 7–9 sessions across 3 mice, Kruskal-Wallis test followed by Tukey-Kramer post hoc tests, chi-square(3,40) = 14.45, p = 0.0024).

$^*p < 0.05$, $^{**}p < 0.01$, $^{***}p < 0.001$. All boxplots show median ± interquartile; whiskers show range excluding outliers. See also Figures S2 and S4.

Please cite this article in press as: Zutshi et al., Extrinsic control and intrinsic computation in the hippocampal CA1 circuit, Neuron (2021), https://doi.org/10.1016/j.neuron.2021.11.015

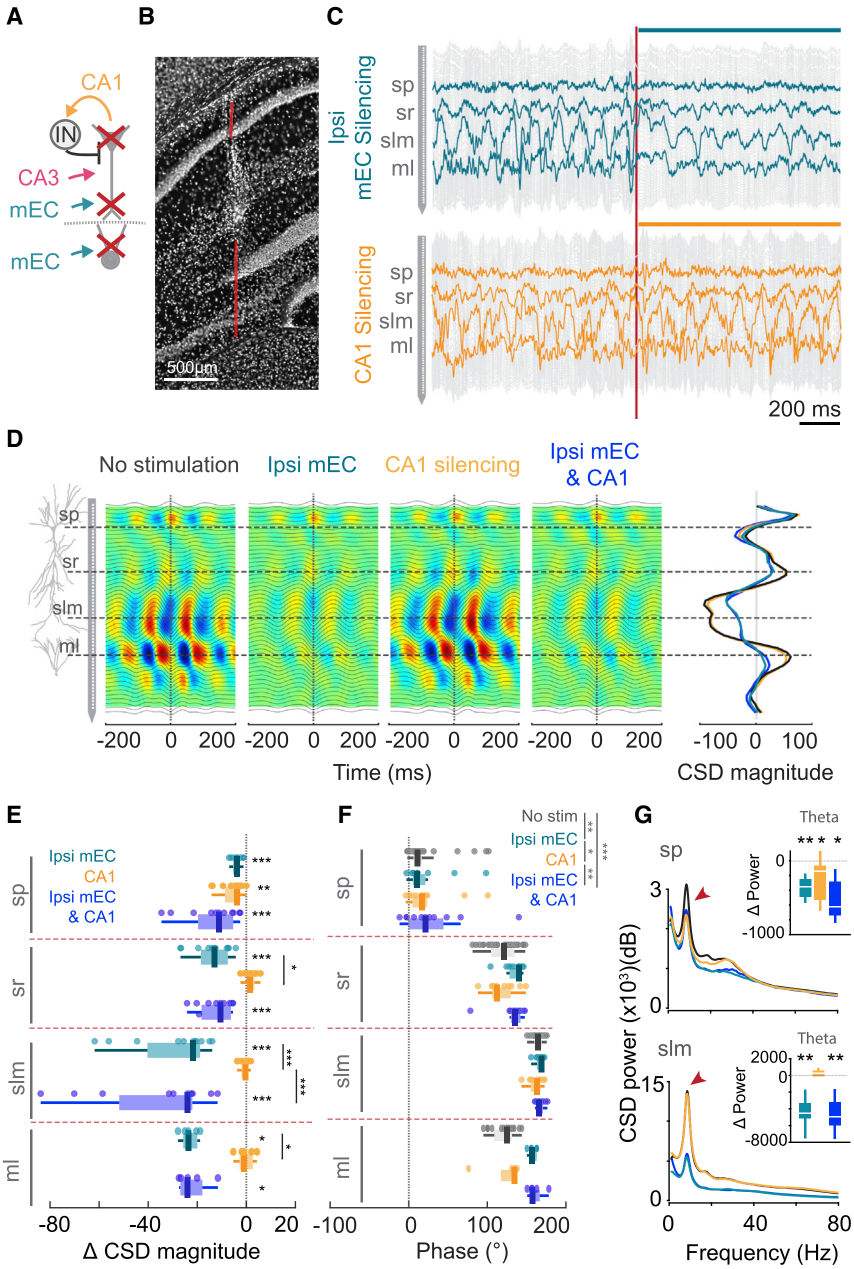

Figure 3. Minimal effect of local CA1 silencing on theta oscillations

(A) Schematic of the silencing strategy.

(B) Track of the linear silicone probe.

(C) 2-s-long LFP traces during ipsi mEC (top) and local CA1 (bottom) silencing. An immediate decrease in theta power was observed upon ipsi mEC silencing. The vertical red line indicates light onset. LFP traces recorded from the sp, sr, sLM, and ml are highlighted.

(D) Average theta CSD profiles during control, ipsi mEC, CA1, and combined silencing. Reduction of sink-source pairs was observed only for manipulations with ipsi mEC silencing. Right: average CSD magnitude at time 0, overlaid across all 4 conditions.

(E) Average change in CSD magnitude across different hippocampal layers for each of the manipulations (each dot represents one session from one animal, n = 11 sessions across 4 mice; within layer: Wilcoxon signed rank test against 0; across layers: 2-way ANOVA followed by Tukey-Kramer post hoc tests; layer-manipulation interaction, F(6,102) = 5.33, $p < 0.001$; only within-layer post hoc results are shown).

(F) Theta phase reversal (with respect to so theta phase) across the sp to the ml was preserved during all manipulations (n = 11 sessions across 4 mice, 2-way ANOVA followed by Tukey-Kramer post hoc tests, layer-manipulation interaction, F(9,212) = 1.83, p = 0.065; manipulation, F(3,212) = 8.44, $p < 0.001$; layer F(3,212) = 461.07, $p < 0.001$; all layers were different from each other, $p < 0.05$).

(G) Left: average power frequency spectra of CSD across all mice (n = 4) upon ipsi mEC, CA1, and combined ipsi mEC and CA1 silencing for the sp and sLM. Red arrows, theta peak. Right: change in theta (6–12 Hz) CSD power for each manipulation compared with baseline in the sp and sLM (n[ipsi mEC, CA1, ipsi mEC and CA1] = 9, 9, and 9 sessions from 4 mice, Wilcoxon two-sided signed rank test against 0; sp: theta, p = 0.004, 0.02, 0.02, respectively; sLM: theta, p = 0.004, 0.16, 0.004, respectively). Color legend as in (E).

*$p < 0.05$, **$p < 0.01$, ***$p < 0.001$. All boxplots show median ± interquartile; whiskers show range excluding outliers. See also Figures S2 and S4.

str. oriens and molecular layer and *str. radiatum* and molecular layer increased during stimulation (Figures S2E and S2F). The gradual theta phase-shift in the *str. radiatum* became steeper, and the coherence minimum between the *str. oriens* and *str. radiatum* theta shifted closer to the pyramidal layer (Figures S2E, S2F, and 4E), similar to results reported previously after surgical removal of the entire entorhinal cortex (Bragin et al., 1995). As an additional control, CSD activity remained mostly unchanged in the (non-stimulated) side arms of the maze between control and stimulation trials (Figure S2C). Optogenetic inactivation of the ipsilateral mEC led to a small but significant deterioration of choice behavior in the maze (Figure S4A).

Effect of local suppression of CA1 pyramidal cells on LFP

Direct optogenetic suppression of CA1 pyramidal cells did not exert a significant effect on the depth distribution of theta currents, except in the pyramidal layer (Figures 3A–3E; n = 4 mice), despite the strong reduction of the discharge frequency of CA1 neurons (Figures 1D, 1E, and S1C). The depth profile of theta phase was not significantly affected (Figure 3F), although a significant decrease in high gamma power (150–300 Hz) was observed (Figures S2L and S2M). When local suppression was combined with simultaneous suppression of mEC neuronal spiking, the effect of the combined optogenetic manipulation on CSD power was largely similar to mEC suppression alone (Figure 3G). Overall,

Please cite this article in press as: Zutshi et al., Extrinsic control and intrinsic computation in the hippocampal CA1 circuit, Neuron (2021), https://doi.org/10.1016/j.neuron.2021.11.015

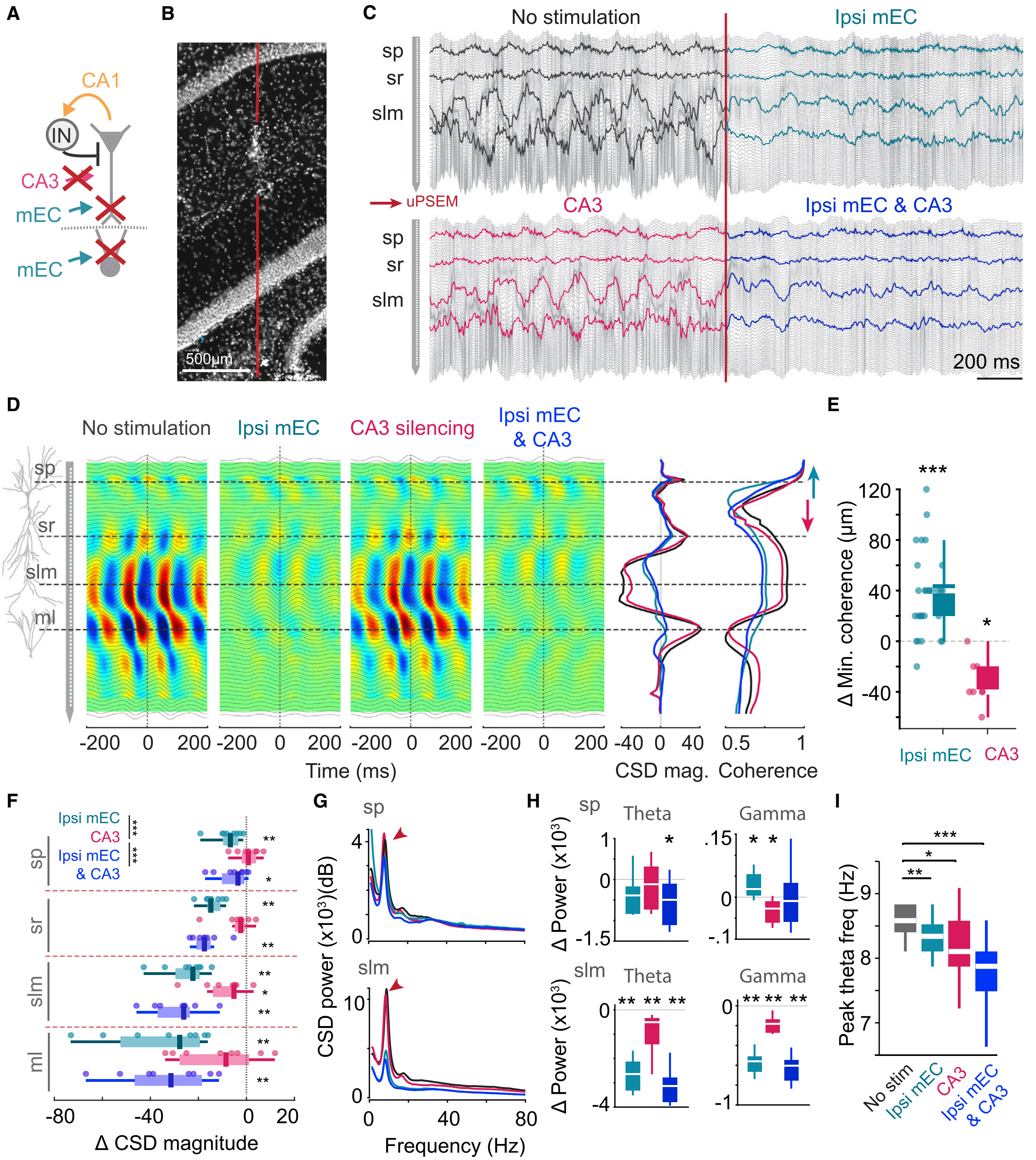

Figure 4. CA3 silencing exerts a minor effect on theta amplitude

(A) Silencing strategy for combined ipsi mEC and bilateral CA3 manipulations.

(B) Track of the linear silicone probe.

(C) 2-s-long LFP traces during ipsi mEC, bilateral CA3, and combined silencing. Highlighted traces correspond to the sp, sr, sLM, and ml.

(D) Average CSD maps of theta oscillations during each manipulation. Note only minor decreases in the CSD magnitude upon CA3 silencing. Center right: average CSD magnitude at time 0, overlaid across all 4 conditions. Right: coherence magnitude along the depth of CA1 with respect to the LFP at the *str. oriens* during each of the manipulations. The minima of LFP coherence between the sp and sr shifted upward during ipsi mEC silencing and downward during CA3 silencing.

(legend continued on next page)

these findings show that firing rates and the magnitude of synaptic currents, as measured by CSD, are dissociable.

Effect of CA3 inactivation on LFP

Because mEC silencing also affected the CA3 region, which, in turn, can influence the CA1 region, we next examined the selective effects of the CA3 input in mice with bilateral PSAM^4-GlyR expression in CA3 pyramidal cells combined with AAV5-mDlx-ChR2-mCherry in the mEC. We tested the effect of optogenetic silencing of the mEC versus CA3 PSAM^4-GlyR silencing and their combined effects. In contrast to optogenetic pulses, PSAM^4-GlyR induction was sustained, affecting hippocampal networks in all aspects of the task. PSAM^4-GlyR-induced suppression of CA3 neuronal activity visibly increased motor activity in the home cage and drastically reduced memory performance in the maze (Figures S4D and S4H). Despite the large spatial extent of the silenced CA3 region, demonstrated by the robust suppression of neuronal firing of CA3 and dentate neurons (Figures 1B, 1F, and S1D), theta currents were not significantly affected, except for a small reduction of the sink in the sLM (Figures 4A–4E). However, phase and phase coherence measures demonstrated a clear effect of CA3 manipulation. Theta phase, relative to the *str. oriens* signal, remained unchanged in the CA1 layers, but the phase shift between the sLM and the dentate molecular layer in the intact animal was abolished by PSAM^4-GlyR treatment (Figure S3I). Opposite to the effect of mEC silencing, the theta coherence minimum between *str. oriens* and *str. radiatum* theta signals shifted deeper in the CA1 *str. radiatum* (Figures 4D, 4E, and S3H). In PSAM^4-GlyR sessions, theta frequency was reduced by approximately 0.5 Hz (Figure 4I), and this reduction could not be explained by a change of locomotion speed (Figures S4I–S4M). The combined effects of PSAM^4-GlyR on CA3 and optogenetic silencing of the mEC on reduction of theta current magnitude and theta frequency were additive (Figures 4F–4I, S4L, and S4M). In contrast to PSAM^4-GlyR sessions, vehicle injection (control sessions) did not induce changes in physiological or behavioral measures (Figures S3B, S3C, and S4D–S4H).

Input-unique effects of transient functional deafferentation on network-embedded firing

The theta phase preference of CA1 pyramidal neurons depends on the relative strength of several phase-shifted theta-modulated inputs (Fernández-Ruiz et al., 2017; Mizuseki et al., 2009). Optogenetic suppression of the mEC slightly advanced the phase preference of CA1 pyramidal cells (Figure 5A) and interneurons (Figure S5A). An opposite-direction small shift of theta phase preference of spiking was observed during local suppression of the CA1 circuits (Figure 5A). In the PSAM^4-GlyR group, pyramidal cells, as a group, advanced their preferred phase by 30°, but many cells shifted as much as 120° from the trough toward the peak of the theta cycle (Figure 5A). With each type of manipulation, the spike-theta phase modulation (“mean vector length”) increased (Figure 5B), implying a reduced distribution of spikes in the theta phase space. A similar effect on preferred theta phase firing was observed for interneurons (Figure S5B). No phase shift was induced in vehicle control sessions (Figure S3G).

Spikes of place cells within their place fields oscillate faster than the simultaneously recorded LFP theta, and the consequence of this frequency difference-induced interference is “phase precession” of spikes (O’Keefe and Recce, 1993). Bilateral mEC and CA3 manipulations led to a 40%–50% decrease in the proportion of significantly precessing place fields (Figures S5C–S5E), suggesting that both of these inputs are required by CA1 pyramidal cells for effective phase precession (Davoudi and Foster, 2019; Fernández-Ruiz et al., 2017; Schlesiger et al., 2015). The slope of the remaining fraction of precessing cells was affected only by the bilateral mEC, not by the CA3 manipulation, and continued to be significantly negative despite all manipulations, suggesting that the deafferented CA1 circuit is capable of supporting some level of phase precession (Figures S5F and S5G).

To measure whether any of these manipulations affected the timing and synchrony of CA1 neural populations, we quantified the expression of CA1 spike assemblies (Lopes-dos-Santos et al., 2013) while the mice were crossing the central arm of the maze. First, assemblies were defined in 25-ms bins (Harris et al., 2003) across no-stimulation and stimulation trials combined, and the stability of assembly expression was compared between baseline and stimulation epochs (Figures 5C–5E). Assemblies detected over the entire session were affected during bilateral mEC, CA1, and CA3 manipulations, with several assemblies increasing or decreasing their expression strength (Figures 5D, 5E, and S5H). To examine whether these manipulations reduced the ability of the CA1 region to form assemblies or whether different assemblies were formed, we identified assemblies independently during baseline and stimulation trials. There

---

(E) Ipsi mEC silencing led to an upward shift of ~40 μm of the coherence minimum (each dot represents one session from one animal, n = 29 sessions from 12 mice, Wilcoxon two-sided signed rank test against 0; $p < 0.001$), whereas CA3 silencing led to a downward shift of ~40 μm (n = 8 sessions from 3 mice, Wilcoxon two-sided signed rank test against 0; $p = 0.0156$).

(F) Average change in CSD magnitude in different hippocampal layers for each of the manipulations (each dot represents one session from one animal, n = 8 sessions across 3 mice; within layer: Wilcoxon signed rank test against 0; across layers: 2-way ANOVA followed by Tukey-Kramer post hoc tests, layer-manipulation interaction, $F(6,84) = 1.14$, $p = 0.35$; manipulation, $F(2,84) = 18.12$, $p < 0.001$; layer, $F(3,84) = 18.49$, $p < 0.001$). CA3 silencing only led to a significant reduction in the sLM.

(G) Average power frequency spectra of sp and sLM CSD across mice (n = 3) upon ipsi mEC, CA3, and combined silencing. Color legend as in (E).

(H) Change in theta (6–12 Hz) and gamma (25–90 Hz) CSD power for each manipulation compared with baseline in sp and sLM (n[ipsi mEC, CA3, ipsi mEC and CA3] = 8, 8, and 8 sessions from 3 mice, Wilcoxon two-sided signed rank test against 0; sp: theta, p = 0.07, 0.46, 0.04, respectively; gamma, p = 0.04, 0.015, 0.74, respectively; sLM: theta, p = 0.008, 0.008, 0.008, respectively; gamma, p = 0.008, 0.008, 0.008, respectively).

(I) CA3 and ipsi mEC silencing led to an ~0.5 Hz decrease in the peak theta oscillation frequency (n = 15 sessions across 6 mice, Friedman test followed by Tukey-Kramer post hoc tests, chi-square(3,42) = 25.33, $p < 0.001$).

*$p < 0.05$, **$p < 0.01$, ***$p < 0.001$. All boxplots show median ± interquartile; whiskers show range excluding outliers. See also Figures S3 and S4.

Please cite this article in press as: Zutshi et al., Extrinsic control and intrinsic computation in the hippocampal CA1 circuit, Neuron (2021), https://doi.org/10.1016/j.neuron.2021.11.015

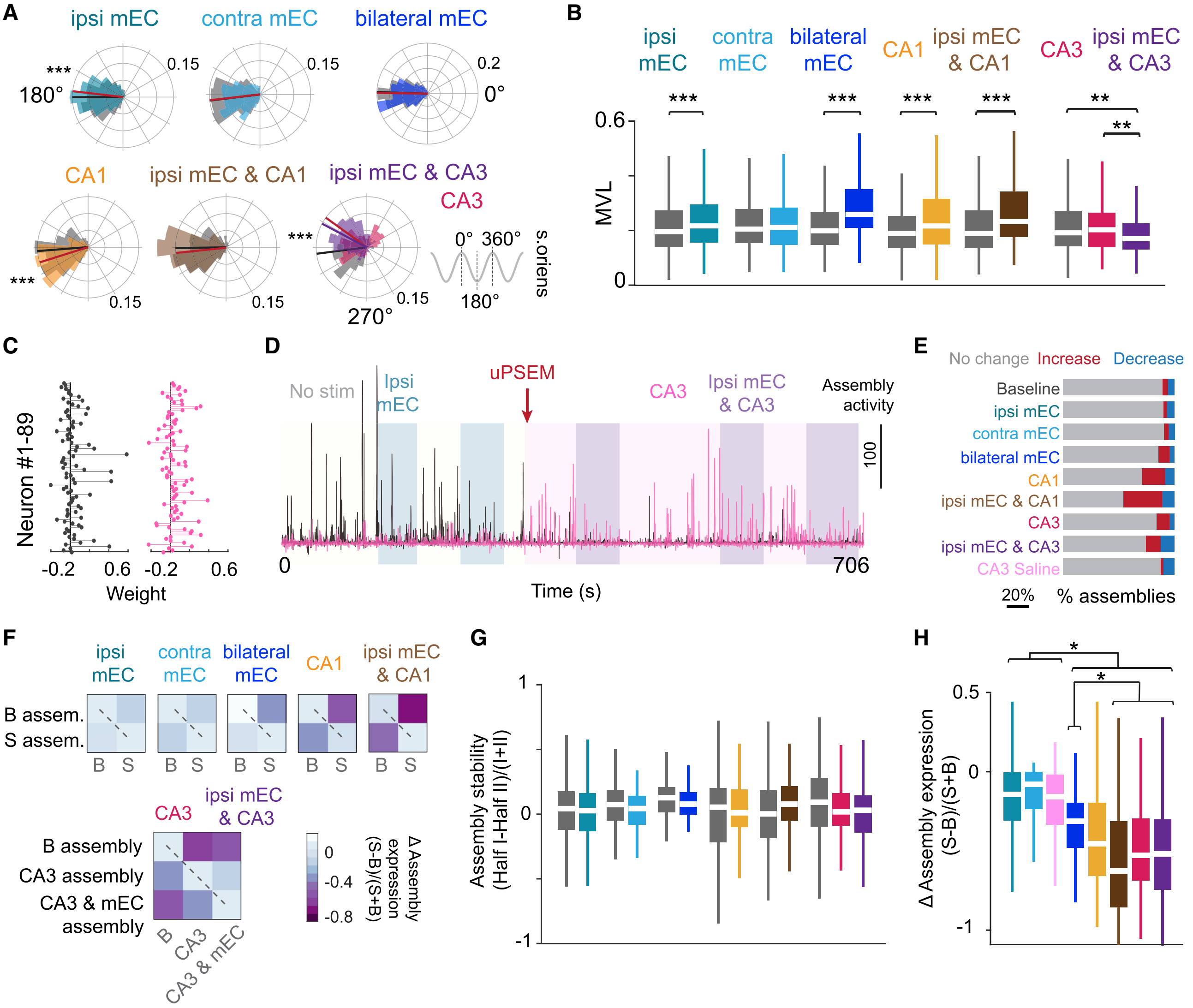

Figure 5. Theta phase preference of spiking is controlled distinctly by inputs

(A) Distribution of theta phase angle preferences of all CA1 pyramidal cells during no stimulation in the central arm compared with each respective manipulation. The radial axis represents probability for each bin. Small but opposite shifts in the phase preference were observed during ipsi mEC and CA1 silencing, whereas CA3 silencing led to an ~30° shift in preferred phase angle. Only cells that were significantly modulated by theta (Rayleigh test, $p < 0.05$) were included in the analysis (Wilcoxon rank-sum test; ipsi mEC, $Z = 3.65$, $p < 0.001$; contra mEC, $Z = 0.145$, $p = 0.885$; bilateral mEC, $Z = -0.316$, $p = 0.752$; CA1, $Z = -3.91$, $p < 0.001$; ipsi mEC and CA1, $Z = -1.24$, $p = 0.216$; CA3, ipsi mEC and CA3, Kruskal-Wallis test followed by Tukey-Kramer post hoc tests, chi-square(2,1054) = 52.06, $p < 0.001$; baseline is significantly different from CA3 and ipsi mEC and CA3, $p < 0.001$). Gray shaded areas (and black lines) are baseline, colored shaded areas (and lines) are stimulation.

(B) Most manipulations resulted in an increase in the mean vector length (MVL) of locking to theta phase for individual cells (Wilcoxon rank-sum test; ipsi mEC, $Z = -5.185$, $p < 0.001$; contra mEC, $Z = 0.115$, $p = 0.908$; bilateral mEC, $Z = -9.57$, $p < 0.001$; CA1, $Z = -4.185$, $p < 0.001$; ipsi mEC & CA1, $Z = -5.45$, $p < 0.001$; CA3, ipsi mEC and CA3, Kruskal-Wallis test followed by Tukey-Kramer post hoc tests, chi-square(2,1054) = 14.84, $p < 0.001$).

(C) The relative weights of each neuron for two example assemblies.

(D) Assembly expression over time of the two assemblies shown in (C). The black assembly is highly expressed during no stimulation and ipsi mEC silencing but is diminished after PSAM inactivation of CA3. The opposite effect is observed for the pink assembly.

(E) Bilateral mEC, CA1, and CA3 manipulations increased or decreased cell assemblies identified during baseline runs (STAR Methods).

(F) Assemblies were defined for the first and second halves of baseline aas well as stimulation sessions separately, and the change in assembly expression was quantified. Baseline and stimulation assemblies had minimal changes in expression between the two halves (i.e., diagonal, dashed line), but assembly expression decreased between conditions (i.e., anti-diagonal).

(G) Assembly stability (comparisons along the diagonal from F) was preserved within all manipulations (Wilcoxon two-sided signed rank test; ipsi mEC, $p = 0.51$; contra mEC, $p = 0.42$; bilateral mEC, $p = 0.155$; CA1, $p = 0.70$; ipsi mEC and CA1, $p = 0.26$; CA3, ipsi mEC and CA3, Kruskal-Wallis test followed by Tukey-Kramer post hoc tests, chi-square(2,402) = 5.75, $p = 0.06$). Color legend as in (B).

(legend continued on next page)

Please cite this article in press as: Zutshi et al., Extrinsic control and intrinsic computation in the hippocampal CA1 circuit, Neuron (2021), https://doi.org/10.1016/j.neuron.2021.11.015

was no change in the number of assemblies or the fraction of highly contributing neurons per assembly during any of the manipulations (Figures S5I and S5J), suggesting that, despite functional deafferentation, the CA1 circuit continued to express cell assemblies. To quantify this effect further, baseline and stimulation trials were divided into halves, and the expression between the two halves demonstrated that assemblies expressed during stimulation were also stable (Figures 5F and 5G). In contrast, the expression of baseline assemblies changed drastically during bilateral mEC, CA1, and CA3 manipulations, suggesting reorganization of co-firing populations of cells (Figure 5H). This result was further supported by examining the pairwise correlation of pyramidal cells and clustering co-firing cells separately during baseline and stimulation sessions (STAR Methods). Although these clusters were maintained between the two halves of baseline and stimulation conditions, there was a complete reorganization of these clusters during bilateral mEC, CA1, and CA3 manipulations (Figures S5K and S5L). These results demonstrate that afferent inputs are valuable in selecting populations of co-firing neurons and that local CA1 manipulation can also reconfigure neuronal assemblies.

Spatial firing of CA1 pyramidal neurons is differentially affected by specific afferents

For maintaining the relationship between CA1 neuronal assemblies and environmental/body cues, we reasoned that at least some input is needed to update the mouse's position in the maze. To address this, we examined how the transient deafferentation perturbations affected the place map. Linearized maps of stimulation and control trials were generated, and maps in the central (stimulated) and side (non-stimulated, control) arm sections of the maze were analyzed separately (Figure 6A). Before and during any of the perturbations, a similar fraction of neurons expressed place fields in the center arm (Figure 6B), suggesting that place field expression is a robust phenomenon and that the CA1 circuit is sufficient to generate place field dynamics with minimal external drive. Optogenetic suppression of the ipsilateral mEC input had a relatively small effect on the stability of place cells, as quantified by the population-vector (PV) correlation (i.e., bin-by-bin correlation of the firing rate of all cells across conditions) and rate-map correlation of individual neurons during control and stimulation trials (Figures 6C–6E). However, the importance of the mEC was clearly revealed when mEC silencing was combined with other perturbations. Combined ipsilateral and contralateral mEC stimulation resulted in a larger decrease than the algebraic sum of the separate manipulations (''supralinear'' effect; Figures 6C and S6C). Local CA1 suppression exerted a larger perturbation on place map stability, which was supralinearly enhanced by mEC co-stimulation (Figures 6D and S6C). These changes can be contrasted to persisting place field stability in the side arms (within-run control of side arms and delay area; Figure 6D). PSAM^4-GlyR-induced suppression of the CA3 region had a profound effect on place field stability across conditions, which was present throughout the maze, because of the continuous presence of the pharmacogenetic ligand (Figure 6E). The strongest remapping of place fields was observed when optogenetic silencing of the mEC was co-applied during CA3 suppression sessions (Figure 6E). However, the remapped field locations on the non-mEC stimulated (side) arm remained stable throughout the recording session despite ongoing CA3 silencing (Figure S3J). These changes were not observed in the vehicle control sessions (Figures S3D–S3F). These profound changes in place field correlations could be dissociated from firing rates because downsampling of spikes under control conditions (STAR Methods) before constructing the rate maps and population vectors yielded comparable within-session map stability differences between control and perturbation conditions (Figures S6E, S6H, and S6K). PSAM^4-GlyR CA3 perturbation and bilateral mEC silencing reduced place field stability, whereas other spatial properties, such as place field size and information (bits/spike), remained largely unaltered even after examining downsampled maps (Figures S6F–S6K).

DISCUSSION

Using a combination of physiological recordings, CSD analyses of the LFP, and optogenetic/pharmacogenetic perturbations, we found that transient deafferentation of the hippocampal network induced differential effects on subthreshold collective activity, as reflected by the LFP, and the firing patterns of individual neurons. The mEC was the main current generator of hippocampal theta oscillations. Input (bilateral CA3 and bilateral mEC) and local (CA1) perturbations resulted in remapping of the CA1 population. However, the fraction of place fields and the ability of the CA1 circuit to support place field activity and express assemblies remained largely intact, even during double deafferentations. These findings suggest that the CA1 network can give rise to substantially more self-organized dynamics that suspected so far.

LFP and neuronal spiking are dissociable

LFP is composed of the summed transmembrane potential changes in synchronously active neurons, brought about mainly by excitatory and inhibitory postsynaptic potentials (EPSPs and IPSPs, respectively) and intrinsic currents of neurons (Buzsáki et al., 2012). Therefore, it characterizes the subthreshold activity of neuronal populations as opposed to their output spiking. Excitatory activity impinges upon the dendrites of pyramidal neurons, whereas the somatic region is contacted by inhibitory synapses (Buhl et al., 1994; Gulyás et al., 1999; Halasy et al., 1996). Of the three manipulations, mEC silencing had the largest effect on LFP, although we would like to add a cautionary note that it is impossible for the efficacy of silencing in each brain region to be identical, and some of the differences in the scale of effects observed may arise from this mismatch. CA3/DG

(H) Bilateral mEC, CA1, and CA3 manipulations led to the largest change in assembly expression across baseline versus manipulated runs (quantification of the top right boxes from each heatmap in F) (Kruskal-Wallis test followed by Tukey-Kramer post hoc tests; chi-square (7,949) = 244.85, $p < 0.001$). Color legend as in (E).

*$p < 0.05$, **$p < 0.01$, ***$p < 0.001$. All boxplots show median ± interquartile; whiskers show range excluding outliers. See also Figure S5.

Please cite this article in press as: Zutshi et al., Extrinsic control and intrinsic computation in the hippocampal CA1 circuit, Neuron (2021), https://doi.org/10.1016/j.neuron.2021.11.015

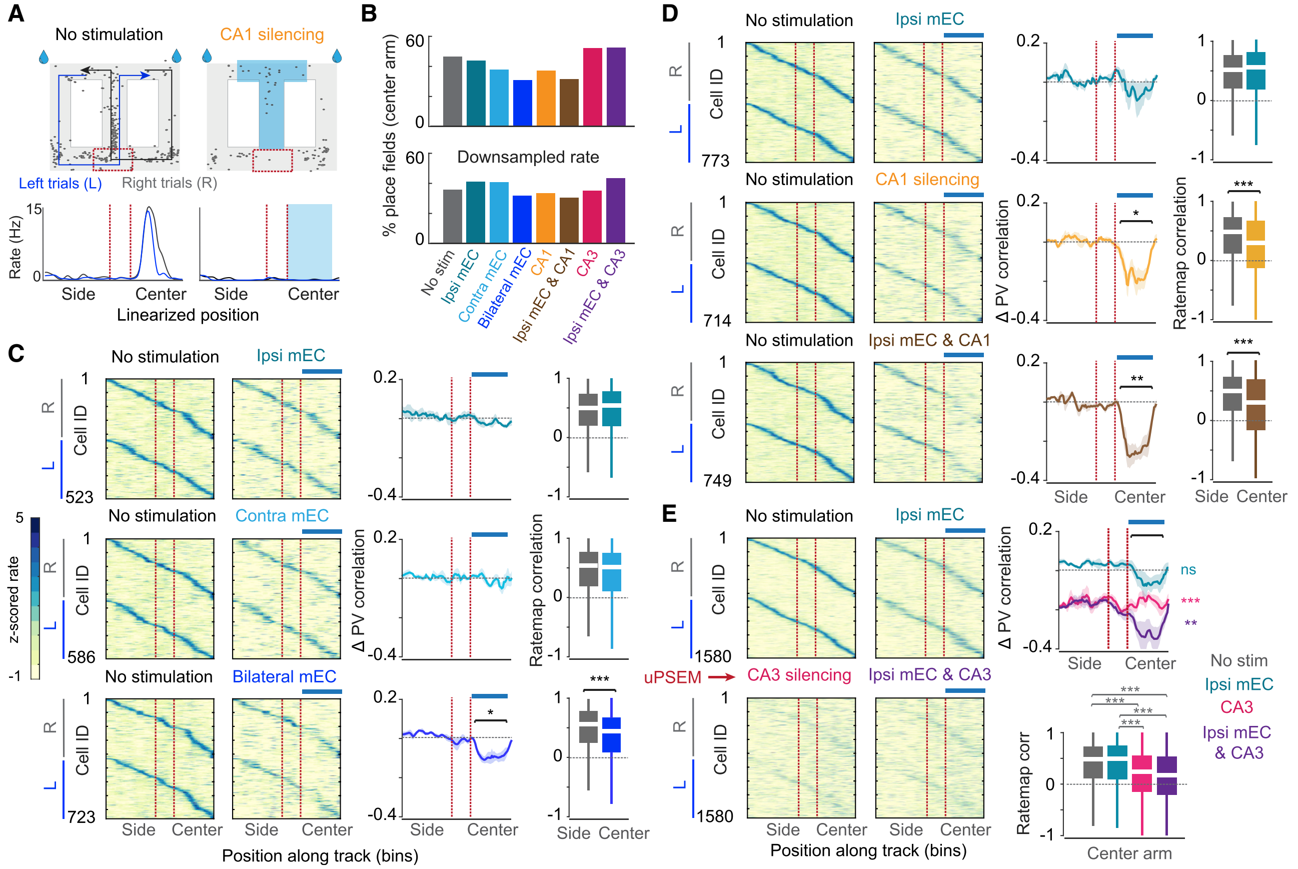

Figure 6. Spatial firing persists after all manipulations despite remapping of fields

(A) Schematic of the spatial alternation task with spikes overlaid (black dots) from an example CA1 pyramidal cell that was targeted during CA1 silencing. The maze was linearized into left and right trials, as depicted by the paths superimposed on the maze. Bottom: average linearized rate map for the same example cell for left and right trials with and without stimulation. Light blue, zone of light stimulation; red dashed lines, delay zone.

(B) Top: percentage of place fields defined in the center arm during baseline and each of the 7 manipulations. Bottom: to account for the rate changes during manipulations, each cell was downsampled during baseline to match the rate during manipulation, and the percentage of place fields was determined in the downsampled maps.

(C) Left: *Z*-scored rate maps sorted separately for left versus right trials during baseline and the corresponding ipsi mEC, contra mEC, and bilateral mEC silencing trials. The blue bar above indicates the targeted stimulation zone (central arm). Place fields are sorted by their position during baseline, and the order is maintained for stimulation sessions. Center: the entire duration of each baseline and stimulation session was divided into two halves, and a position bin-by-bin correlation across all cells (PV correlation) was calculated between the half-session baseline maps. The same value was calculated between baseline and stimulation trials and normalized to the baseline PV correlation. A significant deterioration in PV correlation was observed during bilateral mEC silencing (one-sample t test against 0, n = 3 mice; ipsi mEC, $p = 0.37$; contra mEC, $p = 0.83$; bilateral mEC, $p = 0.045$). Right: cell-by-cell rate map correlation for the center arm during baseline (gray), and baseline versus stimulation (colored) revealed significant remapping during bilateral mEC silencing (Wilcoxon signed rank test; ipsi mEC, $p = 0.21$; contra mEC, $p = 0.06$; bilateral mEC, $p < 0.001$).

(D) Same as (C), but for ipsi mEC, CA1, and combined silencing. There was a significant decrease in PV correlation during CA1 and combined silencing (n = 5 mice; ipsi mEC, $p = 0.57$; CA1, $p = 0.023$; ipsi mEC and CA1, $p = 0.003$). A significant change in the rate map correlation was observed during all manipulations (Wilcoxon signed rank test; ipsi mEC, $p = 0.10$; CA1, $p < 0.001$; bilateral mEC, $p < 0.001$).

(E) Same as (C) and (D) but for ipsi mEC, bilateral CA3, and combined manipulations. The CA3 manipulation was targeted to the entire maze because of the continuous nature of the pharmacogenetic manipulation. Strong remapping was observed during CA3 silencing, which was further altered by additional ipsi mEC silencing (central arm, n = 6 mice, One sample t test against 0; ipsi mEC, $p = 0.21$; CA3, $p < 0.001$; ipsi mEC and CA3, $p = 0.0012$). A significant change in the rate map correlation was also observed during all manipulations (central arm, Kruskal-Wallis test followed by Tukey-Kramer post hoc tests, chi-square(3,6289) = 358.4882, $p < 0.001$).

*$p < 0.05$, **$p < 0.01$, ***$p < 0.001$. All boxplots show median ± interquartile; whiskers show range excluding outliers. See also Figure S6.

neurons strongly decreased their firing rates, coupled with decreased theta power in the molecular layer and hilus. Stellate cells in layer 2 of the mEC, but not other mEC neurons, are tuned to resonate at theta frequency *in vivo* (Quilichini et al., 2010), mainly because of a prominent HCN1 channel-mediated h current (Alonso and Llinás, 1989; Giocomo and Hasselmo, 2009; Giocomo et al., 2011; Isomura et al., 2006). Electric stimulation of mEC axons induces large extracellular PSPs and population spikes of granule cells (Andersen et al., 1971). Overall, these observations suggest that the main current source of theta activity

Please cite this article in press as: Zutshi et al., Extrinsic control and intrinsic computation in the hippocampal CA1 circuit, Neuron (2021), https://doi.org/10.1016/j.neuron.2021.11.015

in the dentate gyrus is AMPA receptor-mediated fast transmission dominantly from mEC stellate cells.

In contrast to the dentate area, optogenetic silencing of the mEC brought about a small effect on the overall firing rates of CA1 pyramidal cells but a dramatic reduction of theta currents, particularly in the sLM, the target of layer 3 mEC pyramidal cells (Amaral and Lavenex, 2007). The depth profile of the theta waves, coherence, and phase in the intact mouse was similar to those described previously in rats (Brankačk et al., 1993; Buzsáki et al., 1983, 1986; Fernández-Ruiz et al., 2021; Kamondi et al., 1998; Lasztóczi and Klausberger, 2016). Although entorhinal synapses on the distal dendrites of pyramidal neurons are larger than excitatory synapses in other layers (Megías et al., 2001), single-pulse stimulation of this path induces only a weak sink in the sLM and fails to elicit spiking in pyramidal cells because of the strong feedforward inhibition (Isomura et al., 2006). On the other hand, repetitive stimulation of the mEC or pairing it with CA3 stimulation is effective because of potentiation of synapses on the distal apical dendrites, depression of entorhinal-interneuron spike transmission (Buzsáki, 2002), and induction of large Ca^{2+} spikes in the distal dendrites of CA1 pyramidal cells (Kamondi et al., 1998; Larkum et al., 1999; Magee and Carruth, 1999; Schiller et al., 1997). Thus, the mechanisms of theta current generation in CA1 are different than in the dentate gyrus.

Direct projections from deep layers of the mEC to the CA1 regions have been described (van Groen et al., 2003; Witter and Amaral, 1991). This weak projection targets the basal dendrites of CA1 pyramidal cells and interneurons in the *str. oriens*. Because our viral infections also targeted interneurons in the deep layers of the mEC, some of the changes we observed in the CA1 *str. oriens* may have been brought about by this complementary input. In addition to excitatory inputs, the mEC also sends direct inhibition to the hippocampus (Melzer et al., 2012; Ye et al., 2018) and to the medial septum (Gulyás et al., 2003). These long-range GABAergic neurons arise mainly in the lateral EC and less so in the mEC (Basu et al., 2016) but are unlikely to contribute significantly to the LFP changes we observed because of their sparsity and because stimulation of their CA1 terminals did not bring about detectable changes in LFP (Figures S2J and S2K). The large differences between ipsilateral and contralateral mEC stimulation also indicates that the effect of mEC-septal projection was not an important contributor to the LFP effects we observed.

In addition to the mEC, afferents from the lateral entorhinal cortex, perirhinal cortex, and thalamic *reuniens* neurons also project to the sLM (Amaral and Lavenex, 2007). Furthermore, the ratio of inhibitory to excitatory synapses is 1 to 4 in the sLM, which is 8-fold higher than in other dendritic layers (Megías et al., 2001). Therefore, the surviving small theta sink source in the proximal part of the layer (Figure 2) may reflect the activity of extrahippocampal inputs (Dolleman-Van der Weel et al., 1997) and/or inhibitory currents from O-LM and sLM-targeting neurogliaform interneurons.

Local silencing of CA1 pyramidal neurons further supports the dissociability of dendritic currents and spiking activity. Although firing rates of local neurons decreased substantially, local silencing reduced theta currents only in the pyramidal layer, leaving the rest of the layers unperturbed, corroborating previous observations in rats, in which pyramidal neurons were strongly silenced pharmacogenetically but theta LFP was not affected (Rogers et al., 2021). Surprisingly, widespread and bilateral suppression of CA3 spiking activity induced only a minor effect on the theta CSD profile, although it had a significant effect on coherence measures. This finding indicates that the LFP/CSD changes in CA1 during mEC suppression were not mediated dominantly by the layer 2-dentate-CA3-CA1 path but by the direct layer 3-to-CA1 projection. A possible explanation for the weak effect of CA3 silencing on the theta sink in the *str. radiatum* is that the reduced excitation similarly affected CA1 pyramidal neurons and the layer-matching bistratified interneurons. In turn, the relatively preserved ratio of excitation and inhibition could produce a comparable transmembrane drive in the CA1 pyramidal cells. The additional role of local interneurons is supported by two findings. First, the gradual phase shift of theta waves from the *str. oriens* to the sLM, assumed to be the result of phase-shifted inputs (Brankačk et al., 1993; Buzsáki, 2002; Buzsáki et al., 1986), was only minimally affected even by combined CA3 and mEC inactivation (Figure S3K), implying that local circuit mechanisms are at play. Second, during local CA1 inactivation, the theta phase preference of the remaining active CA1 pyramidal cells shifted significantly. To identify the exact mechanisms of CSD and coherence changes will require further experiments, targeting the different interneuron types.

Our results also suggest that cell assemblies in the entorhinal cortex-hippocampus regions contribute to theta frequency as well. Suppression of mEC and CA3 inputs reduced theta frequency (Ormond and McNaughton, 2015; Schlesiger et al., 2015). A potential mechanism of this effect is the hippocampo-septal feedback. Assemblies of place cells, oscillating at the same frequency, may enslave their associated long-range inhibitory interneurons, whose septal collaterals (Gulyás et al., 2003) can adjust the frequency of septal theta pacemaker neurons. This way the oscillation frequency of place cell assemblies may adjust the global LFP theta rhythm (Geisler et al., 2010).

Intrinsic computation in the CA1 network

The most surprising finding of our experiments is the contrast between the robust reconfiguration of the relationship between neuronal assemblies and the animal's spatial position by perturbations (i.e., the case of ''remapping'') versus the continued ability of the CA1 network to induce and maintain a new map during various forms of functional disconnections. This conclusion is in contrast to suggestions that CA1 neurons largely inherit their firing patterns and spatial features from their upstream CA3 and EC networks (Ahmed and Mehta, 2009; Brun et al., 2008; Franzius et al., 2007; Rolls et al., 2006; Savelli and Knierim, 2010; Solstad et al., 2006; Steffenach et al., 2005) and that the contribution of the CA1 circuit is mainly to refine the place fields (Mizumori et al., 1989).

Local CA1 silencing, CA3 inactivation, and bilateral mEC inactivation altered cell assembly configurations (Figure 5) and decreased population vector correlations and spatial correlations of individual CA1 neurons (Figure 6), independent of firing rate reductions (Figure S6). CA3 inactivation and local CA1 perturbation exerted a larger effect on the spatial map than

Please cite this article in press as: Zutshi et al., Extrinsic control and intrinsic computation in the hippocampal CA1 circuit, Neuron (2021), https://doi.org/10.1016/j.neuron.2021.11.015

mEC silencing. However, the importance of the mEC (Fernández-Ruiz et al., 2021; Hales et al., 2014; Miao et al., 2015; Miller and Best, 1980; Ormond and McNaughton, 2015; Robinson et al., 2017; Rueckemann et al., 2016; Schlesiger et al., 2015) was clearly demonstrated when ipsilateral mEC perturbation was combined with additional perturbation. The large differences between the effect of the mEC and CA3 inactivation on LFP/CSD and place map reorganization is surprising in light of our finding that mEC silencing was accompanied by a strong disfacilitation of the dentate/CA3 regions.

mEC silencing may be viewed as a combined deafferentation of CA1 neurons from mEC and CA3 inputs (i.e., direct and indirect paths). However, our results do not support such interpretation for theta currents (Figures 2, 3, and 4) or neuronal firing. This apparent paradox may be explained by assuming two parallel pathways from the mEC to CA1. Previous research has shown that there are two distinct types of CA3 pyramidal neurons, one that receives mossy synapses from granule cells (“thorny” type) and another type (“athorny” pyramid cell) that lacks mossy fiber input but gives rise to extensive recurrent and association path collaterals, and the subcircuits formed from these respective populations antagonize each other (Hunt et al., 2018). Although our pharmacogenetic manipulation may have equally affected both CA3 neuron types, mEC inactivation more likely affected thorny CA3 pyramidal cells with granule cell contacts. This hypothesis is supported by the larger effect of the combined mEC and CA3 silencing on DG/CA3 firing rates compared with their individual manipulation (Figures 1G and 1J) and that mEC and CA3 manipulations affected different sets of CA3/DG neurons (Figure S3K). We hypothesize that the subnetwork of CA3 neurons with strongly interconnected recurrent collaterals is more critical for maintaining the place representation of CA1 pyramidal cells than the mEC input. This result is supported by our observation that the stability of the reconfigured CA1 map after CA3 inactivation was diminished. In simple situations, such as walking on the center arm of the maze, environmental cues might not be critical to maintain cell assembly sequences. Only occasional realignment of the internally generated map may be needed, which may be accomplished by mEC or other inputs from retrohippocampal structures (van Strien et al., 2009; Zhang et al., 2013). On the other hand, the outcome may be different in more complex environments when the animal has to rely heavily on multiple landmarks and their relationships. The magnitude of dependence from environmental cues may be one key source of the variability observed across studies examining the effect of the mEC on CA1 neuronal firing patterns (Hales et al., 2014; Ravassard et al., 2013; Robinson et al., 2017; Rueckemann et al., 2016; Schlesiger et al., 2015, 2018; Sharif et al., 2021).

In contrast to the remapping effects of the input and local perturbations (Kanter et al., 2017; Miao et al., 2015; Rueckemann et al., 2016), the transiently deafferented CA1 continued to induce and maintain place fields. These findings suggest that the CA1 region possesses the necessary circuit dynamics to create and maintain sequentially organized neuronal assemblies, a prerequisite for place field sequences. This suggestion is supported by previous observations showing that the participating neurons and their sequences in hippocampal SPW-Rs are largely created by local CA1 circuits without the need for extrinsic inputs (Stark et al., 2015). Further, when animals are tested in novel environments, CA1 neurons remap faster than CA3 neurons (Dong et al., 2021; Frank et al., 2004; Roth et al., 2012), again suggesting that operations in CA3 and CA1 circuits can be independent. Place fields have been suggested to emerge as a result of a hypothetical “attractor” based on extensive excitatory recurrency in the CA3 region (Hunt et al., 2018; Samsonovich and McNaughton, 1997). However, recent computational efforts demonstrated that such a property can also emerge in a model layer 2 mEC network with no recurrent excitation but mutual lateral inhibition (Couey et al., 2013; Pastoll et al., 2013), a requirement present in the CA1 circuit (Freund and Buzsáki, 1996). Overall, our findings suggest that the CA1 circuit is endowed with the computational capacity to generate assembly sequences, detected as sequentially active place fields during maze performance.

STAR★METHODS

Detailed methods are provided in the online version of this paper and include the following:

- KEY RESOURCES TABLE
- RESOURCE AVAILABILITY
  - ○ Lead contact
  - ○ Materials availability
  - ○ Data and code availability
- EXPERIMENTAL MODEL AND SUBJECT DETAILS
- METHOD DETAILS
  - ○ Subjects and surgical procedures
  - ○ Recordings and behavior
  - ○ Unit clustering and neuron classification
  - ○ Ripple detection
  - ○ CSD and coherence analysis
  - ○ Theta phase locking, phase precession, and oscillation frequency analysis
  - ○ Assembly analysis
  - ○ Place field analysis
- QUANTIFICATION AND STATISTICAL ANALYSIS
  - ○ Statistical analysis

SUPPLEMENTAL INFORMATION

Supplemental information can be found online at https://doi.org/10.1016/j.neuron.2021.11.015.

ACKNOWLEDGMENTS

We thank M. Sabariego, K. McClain, N. Nitzan, R. Swanson, D. Tingley, Y. Zhang, and all members of the Buzsáki lab for insightful comments and suggestions for the manuscript. This work was supported by a Leon Levy Neuroscience Fellowship Grant (to I.Z.), NIH grants (R01MH122391, U19NS104590, and U19NS107616), and NSF 1707316 (NeuroNex MINT to Euisik Yoon).

AUTHOR CONTRIBUTIONS

I.Z., A.F.-R., and G.B. conceived and designed the experiments. I.Z. performed all experiments. I.Z. and M.V. analyzed data. I.Z. and G.B. wrote the manuscript with input from all authors.

DECLARATION OF INTERESTS

G.B. is a member of *Neuron*'s advisory board.

Received: August 12, 2021
Revised: October 1, 2021
Accepted: November 12, 2021
Published: December 9, 2021

REFERENCES

Ahmed, O.J., and Mehta, M.R. (2009). The hippocampal rate code: anatomy, physiology and theory. Trends Neurosci. *32*, 329–338.

Ainge, J.A., van der Meer, M.A.A., Langston, R.F., and Wood, E.R. (2007). Exploring the role of context-dependent hippocampal activity in spatial alternation behavior. Hippocampus *17*, 988–1002.

Alonso, A., and Llinás, R.R. (1989). Subthreshold Na+-dependent theta-like rhythmicity in stellate cells of entorhinal cortex layer II. Nature *342*, 175–177.

Amaral, D., and Lavenex, P. (2007). Hippocampal Neuroanatomy BT - The Hippocampus Book (Oxford University Press).

Andersen, P., Bliss, T.V.P., and Skrede, K.K. (1971). Lamellar organization of hippocampal pathways. Exp. Brain Res. *13*, 222–238.

Basu, J., Zaremba, J.D., Cheung, S.K., Hitti, F.L., Zemelman, B.V., Losonczy, A., and Siegelbaum, S.A. (2016). Gating of hippocampal activity, plasticity, and memory by entorhinal cortex long-range inhibition. Science *351*, aaa5694.

Berens, P. (2009). CircStat : A MATLAB Toolbox for Circular Statistics. J. Stat. Softw. *31*, 1–21.

Bezaire, M.J., and Soltesz, I. (2013). Quantitative assessment of CA1 local circuits: knowledge base for interneuron-pyramidal cell connectivity. Hippocampus *23*, 751–785.

Bragin, A., Jandó, G., Nádasdy, Z., Hetke, J., Wise, K., and Buzsáki, G. (1995). Gamma (40-100 Hz) oscillation in the hippocampus of the behaving rat. J. Neurosci. *15*, 47–60.

Brankačk, J., Stewart, M., and Fox, S.E. (1993). Current source density analysis of the hippocampal theta rhythm: associated sustained potentials and candidate synaptic generators. Brain Res. *615*, 310–327.

Brun, V.H., Otnass, M.K., Molden, S., Steffenach, H.A., Witter, M.P., Moser, M.B., and Moser, E.I. (2002). Place cells and place recognition maintained by direct entorhinal-hippocampal circuitry. Science *296*, 2243–2246.

Brun, V.H., Leutgeb, S., Wu, H.Q., Schwarcz, R., Witter, M.P., Moser, E.I., and Moser, M.B. (2008). Impaired spatial representation in CA1 after lesion of direct input from entorhinal cortex. Neuron *57*, 290–302.

Buhl, E.H., Halasy, K., and Somogyi, P. (1994). Diverse sources of hippocampal unitary inhibitory postsynaptic potentials and the number of synaptic release sites. Nature *368*, 823–828.

Buzsáki, G. (2002). Theta oscillations in the hippocampus. Neuron *33*, 325–340.

Buzsáki, G., Leung, L.W., and Vanderwolf, C.H. (1983). Cellular bases of hippocampal EEG in the behaving rat. Brain Res. *287*, 139–171.

Buzsáki, G., Czopf, J., Kondákor, I., and Kellényi, L. (1986). Laminar distribution of hippocampal rhythmic slow activity (RSA) in the behaving rat: current-source density analysis, effects of urethane and atropine. Brain Res. *365*, 125–137.

Buzsáki, G., Anastassiou, C.A., and Koch, C. (2012). The origin of extracellular fields and currents–EEG, ECoG, LFP and spikes. Nat. Rev. Neurosci. *13*, 407–420.

Chenani, A., Sabariego, M., Schlesiger, M.I., Leutgeb, J.K., Leutgeb, S., and Leibold, C. (2019). Hippocampal CA1 replay becomes less prominent but more rigid without inputs from medial entorhinal cortex. Nat. Commun. *10*, 1341.

Couey, J.J., Witoelar, A., Zhang, S.J., Zheng, K., Ye, J., Dunn, B., Czajkowski, R., Moser, M.B., Moser, E.I., Roudi, Y., and Witter, M.P. (2013). Recurrent inhibitory circuitry as a mechanism for grid formation. Nat. Neurosci. *16*, 318–324.

Davoudi, H., and Foster, D.J. (2019). Acute silencing of hippocampal CA3 reveals a dominant role in place field responses. Nat. Neurosci. *22*, 337–342.

Deuchars, J., and Thomson, A.M. (1996). CA1 pyramid-pyramid connections in rat hippocampus in vitro: dual intracellular recordings with biocytin filling. Neuroscience *74*, 1009–1018.

Dolleman-Van der Weel, M.J., Lopes da Silva, F.H., and Witter, M.P. (1997). Nucleus reuniens thalami modulates activity in hippocampal field CA1 through excitatory and inhibitory mechanisms. J. Neurosci. *17*, 5640–5650.

Dong, C., Madar, A.D., and Sheffield, M.E.J. (2021). Distinct place cell dynamics in CA1 and CA3 encode experience in new environments. Nat. Commun. *12*, 2977.

Dragoi, G., and Buzsáki, G. (2006). Temporal encoding of place sequences by hippocampal cell assemblies. Neuron *50*, 145–157.

El-Gaby, M., Reeve, H.M., Lopes-Dos-Santos, V., Campo-Urriza, N., Perestenko, P.V., Morley, A., Strickland, L.A.M., Lukács, I.P., Paulsen, O., and Dupret, D. (2021). An emergent neural coactivity code for dynamic memory. Nat. Neurosci. *24*, 694–704.

Fernández-Ruiz, A., Oliva, A., Nagy, G.A., Maurer, A.P., Berényi, A., and Buzsáki, G. (2017). Entorhinal-CA3 Dual-Input Control of Spike Timing in the Hippocampus by Theta-Gamma Coupling. Neuron *93*, 1213–1226.e5.

Fernández-Ruiz, A., Oliva, A., Soula, M., Rocha-Almeida, F., Nagy, G.A., Martin-Vazquez, G., and Buzsáki, G. (2021). Gamma rhythm communication between entorhinal cortex and dentate gyrus neuronal assemblies. Science *372*, eabf3119.

Frank, L.M., Stanley, G.B., and Brown, E.N. (2004). Hippocampal plasticity across multiple days of exposure to novel environments. J. Neurosci. *24*, 7681–7689.

Franzius, M., Vollgraf, R., and Wiskott, L. (2007). From grids to places. J. Comput. Neurosci. *22*, 297–299.

Freund, T.F., and Buzsáki, G. (1996). Interneurons of the hippocampus. Hippocampus *6*, 347–470.

Geisler, C., Diba, K., Pastalkova, E., Mizuseki, K., Royer, S., and Buzsáki, G. (2010). Temporal delays among place cells determine the frequency of population theta oscillations in the hippocampus. Proc. Natl. Acad. Sci. USA *107*, 7957–7962.

Giocomo, L.M., and Hasselmo, M.E. (2009). Knock-out of HCN1 subunit flattens dorsal-ventral frequency gradient of medial entorhinal neurons in adult mice. J. Neurosci. *29*, 7625–7630.

Giocomo, L.M., Hussaini, S.A., Zheng, F., Kandel, E.R., Moser, M.B., and Moser, E.I. (2011). Grid cells use HCN1 channels for spatial scaling. Cell *147*, 1159–1170.

Gulyás, A.I., Megías, M., Emri, Z., and Freund, T.F. (1999). Total number and ratio of excitatory and inhibitory synapses converging onto single interneurons of different types in the CA1 area of the rat hippocampus. J. Neurosci. *19*, 10082–10097.

Gulyás, A.I., Hájos, N., Katona, I., and Freund, T.F. (2003). Interneurons are the local targets of hippocampal inhibitory cells which project to the medial septum. Eur. J. Neurosci. *17*, 1861–1872.

Hafting, T., Fyhn, M., Molden, S., Moser, M.B., and Moser, E.I. (2005). Microstructure of a spatial map in the entorhinal cortex. Nature *436*, 801–806.

Halasy, K., Buhl, E.H., Lörinczi, Z., Tamás, G., and Somogyi, P. (1996). Synaptic target selectivity and input of GABAergic basket and bistratified interneurons in the CA1 area of the rat hippocampus. Hippocampus *6*, 306–329.

Hales, J.B., Schlesiger, M.I., Leutgeb, J.K., Squire, L.R., Leutgeb, S., and Clark, R.E. (2014). Medial entorhinal cortex lesions only partially disrupt hippocampal place cells and hippocampus-dependent place memory. Cell Rep. *9*, 893–901.

Harris, K.D., Csicsvari, J., Hirase, H., Dragoi, G., and Buzsáki, G. (2003). Organization of cell assemblies in the hippocampus. Nature *424*, 552–556.

Hunt, D.L., Linaro, D., Si, B., Romani, S., and Spruston, N. (2018). A novel pyramidal cell type promotes sharp-wave synchronization in the hippocampus. Nat. Neurosci. *21*, 985–995.

Isomura, Y., Sirota, A., Özen, S., Montgomery, S., Mizuseki, K., Henze, D.A., and Buzsáki, G. (2006). Integration and segregation of activity in entorhinal-hippocampal subregions by neocortical slow oscillations. Neuron *52*, 871–882.

Kamondi, A., Acsády, L., Wang, X.J., and Buzsáki, G. (1998). Theta oscillations in somata and dendrites of hippocampal pyramidal cells in vivo: activity-dependent phase-precession of action potentials. Hippocampus *8*, 244–261.

Kanter, B.R., Lykken, C.M., Avesar, D., Weible, A., Dickinson, J., Dunn, B., Borgesius, N.Z., Roudi, Y., and Kentros, C.G. (2017). A Novel Mechanism for the Grid-to-Place Cell Transformation Revealed by Transgenic Depolarization of Medial Entorhinal Cortex Layer II. Neuron *93*, 1480–1492.e6.

Keinath, A.T., Nieto-Posadas, A., Robinson, J.C., and Brandon, M.P. (2020). DG-CA3 circuitry mediates hippocampal representations of latent information. Nat. Commun. *11*, 3026.

Larkum, M.E., Zhu, J.J., and Sakmann, B. (1999). A new cellular mechanism for coupling inputs arriving at different cortical layers. Nature *398*, 338–341.

Lasztóczi, B., and Klausberger, T. (2016). Hippocampal Place Cells Couple to Three Different Gamma Oscillations during Place Field Traversal. Neuron *91*, 34–40.

Latuske, P., Kornienko, O., Kohler, L., and Allen, K. (2018). Hippocampal remapping and its entorhinal origin. Front. Behav. Neurosci. *11*, 253.

Li, X.-G., Somogyi, P., Ylinen, A., and Buzsáki, G. (1994). The hippocampal CA3 network: an in vivo intracellular labeling study. J. Comp. Neurol. *339*, 181–208.

Lopes-dos-Santos, V., Ribeiro, S., and Tort, A.B.L. (2013). Detecting cell assemblies in large neuronal populations. J. Neurosci. Methods *220*, 149–166.

Magee, J.C., and Carruth, M. (1999). Dendritic voltage-gated ion channels regulate the action potential firing mode of hippocampal CA1 pyramidal neurons. J. Neurophysiol. *82*, 1895–1901.

Magnus, C.J., Lee, P.H., Bonaventura, J., Zemla, R., Gomez, J.L., Ramirez, M.H., Hu, X., Galvan, A., Basu, J., Michaelides, M., and Sternson, S.M. (2019). Ultrapotent chemogenetics for research and potential clinical applications. Science *364*, eaav5282.

Mahn, M., Gibor, L., Patil, P., Cohen-Kashi Malina, K., Oring, S., Printz, Y., Levy, R., Lampl, I., and Yizhar, O. (2018). High-efficiency optogenetic silencing with soma-targeted anion-conducting channelrhodopsins. Nat. Commun. *9*, 4125.

Makarov, V.A., Makarova, J., and Herreras, O. (2010). Disentanglement of local field potential sources by independent component analysis. J. Comput. Neurosci. *29*, 445–457.

McKenzie, S., Huszár, R., English, D.F., Kim, K., Christensen, F., Yoon, E., and Buzsáki, G. (2021). Preexisting hippocampal network dynamics constrain optogenetically induced place fields. Neuron *109*, 1040–1054.e7.

Megías, M., Emri, Z., Freund, T.F., and Gulyás, A.I. (2001). Total number and distribution of inhibitory and excitatory synapses on hippocampal CA1 pyramidal cells. Neuroscience *102*, 527–540.

Melzer, S., Michael, M., Caputi, A., Eliava, M., Fuchs, E.C., Whittington, M.A., and Monyer, H. (2012). Long-range-projecting GABAergic neurons modulate inhibition in hippocampus and entorhinal cortex. Science *335*, 1506–1510.

Miao, C., Cao, Q., Ito, H.T., Yamahachi, H., Witter, M.P., Moser, M.B., and Moser, E.I. (2015). Hippocampal Remapping after Partial Inactivation of the Medial Entorhinal Cortex. Neuron *88*, 590–603.

Middleton, S.J., and McHugh, T.J. (2016). Silencing CA3 disrupts temporal coding in the CA1 ensemble. Nat. Neurosci. *19*, 945–951.

Miller, V.M., and Best, P.J. (1980). Spatial correlates of hippocampal unit activity are altered by lesions of the fornix and endorhinal cortex. Brain Res. *194*, 311–323.

Mitzdorf, U. (1985). Current source-density method and application in cat cerebral cortex: investigation of evoked potentials and EEG phenomena. Physiol. Rev. *65*, 37–100.

Mizumori, S.J.Y., McNaughton, B.L., Barnes, C.A., and Fox, K.B. (1989). Preserved spatial coding in hippocampal CA1 pyramidal cells during reversible suppression of CA3c output: evidence for pattern completion in hippocampus. J. Neurosci. *9*, 3915–3928.

Mizuseki, K., Sirota, A., Pastalkova, E., and Buzsáki, G. (2009). Theta oscillations provide temporal windows for local circuit computation in the entorhinal-hippocampal loop. Neuron *64*, 267–280.

Mizuseki, K., Diba, K., Pastalkova, E., and Buzsáki, G. (2011). Hippocampal CA1 pyramidal cells form functionally distinct sublayers. Nat. Neurosci. *14*, 1174–1181.

Nakashiba, T., Young, J.Z., McHugh, T.J., Buhl, D.L., and Tonegawa, S. (2008). Transgenic inhibition of synaptic transmission reveals role of CA3 output in hippocampal learning. Science *319*, 1260–1264.

Nakashiba, T., Buhl, D.L., McHugh, T.J., and Tonegawa, S. (2009). Hippocampal CA3 output is crucial for ripple-associated reactivation and consolidation of memory. Neuron *62*, 781–787.

O'Keefe, J., and Recce, M.L. (1993). Phase relationship between hippocampal place units and the EEG theta rhythm. Hippocampus *3*, 317–330.

Ormond, J., and McNaughton, B.L. (2015). Place field expansion after focal MEC inactivations is consistent with loss of Fourier components and path integrator gain reduction. Proc. Natl. Acad. Sci. USA *112*, 4116–4121.

Pachitariu, M., Steinmetz, N., Kadir, S., Carandini, M., and Harris, K. (2016). Fast and accurate spike sorting of high-channel count probes with KiloSort. Advances in Neural Information Processing Systems, 4455–4463.

Pastoll, H., Solanka, L., van Rossum, M.C.W., and Nolan, M.F. (2013). Feedback inhibition enables θ-nested γ oscillations and grid firing fields. Neuron *77*, 141–154.

Petersen, P., Siegle, J., Steinmetz, N., Mahallati, S., and Buzsáki, G. (2020). CellExplorer: a graphical user interface and a standardized pipeline for visualizing and characterizing single neurons. Neuron *109*, P3594–P3608.

Quilichini, P., Sirota, A., and Buzsáki, G. (2010). Intrinsic circuit organization and theta-gamma oscillation dynamics in the entorhinal cortex of the rat. J. Neurosci. *30*, 11128–11142.

Ravassard, P., Kees, A., Willers, B., Ho, D., Aharoni, D.A., Cushman, J., Aghajan, Z.M., and Mehta, M.R. (2013). Multisensory control of hippocampal spatiotemporal selectivity. Science *340*, 1342–1346.

Ritchey, M., Libby, L.A., and Ranganath, C. (2015). Cortico-hippocampal systems involved in memory and cognition: the PMAT framework. Prog. Brain Res. *219*, 45–64.

Robinson, N.T.M., Priestley, J.B., Rueckemann, J.W., Garcia, A.D., Smeglin, V.A., Marino, F.A., and Eichenbaum, H. (2017). Medial Entorhinal Cortex Selectively Supports Temporal Coding by Hippocampal Neurons. Neuron *94*, 677–688.e6.

Rogers, S., Rozman, P.A., Valero, M., Doyle, W.K., and Buzsáki, G. (2021). Mechanisms and plasticity of chemogenically induced interneuronal suppression of principal cells. Proc. Natl. Acad. Sci. USA *118*, e2014157118.

Rolls, E.T., Stringer, S.M., and Elliot, T. (2006). Entorhinal cortex grid cells can map to hippocampal place cells by competitive learning. Network *17*, 447–465.

Roth, E.D., Yu, X., Rao, G., and Knierim, J.J. (2012). Functional differences in the backward shifts of CA1 and CA3 place fields in novel and familiar environments. PLoS ONE *7*, e36035.

Rueckemann, J.W., DiMauro, A.J., Rangel, L.M., Han, X., Boyden, E.S., and Eichenbaum, H. (2016). Transient optogenetic inactivation of the medial entorhinal cortex biases the active population of hippocampal neurons. Hippocampus *26*, 246–260.

Sabariego, M., Schönwald, A., Boublil, B.L., Zimmerman, D.T., Ahmadi, S., Gonzalez, N., Leibold, C., Clark, R.E., Leutgeb, J.K., and Leutgeb, S. (2019). Time Cells in the Hippocampus Are Neither Dependent on Medial Entorhinal

Cortex Inputs nor Necessary for Spatial Working Memory. Neuron *102*, 1235–1248.e5.

Samsonovich, A., and McNaughton, B.L. (1997). Path integration and cognitive mapping in a continuous attractor neural network model. J. Neurosci. *17*, 5900–5920.

Savelli, F., and Knierim, J.J. (2010). Hebbian analysis of the transformation of medial entorhinal grid-cell inputs to hippocampal place fields. J. Neurophysiol. *103*, 3167–3183.

Schiller, J., Schiller, Y., Stuart, G., and Sakmann, B. (1997). Calcium action potentials restricted to distal apical dendrites of rat neocortical pyramidal neurons. J. Physiol. *505*, 605–616.

Schlesiger, M.I., Cannova, C.C., Boublil, B.L., Hales, J.B., Mankin, E.A., Brandon, M.P., Leutgeb, J.K., Leibold, C., and Leutgeb, S. (2015). The medial entorhinal cortex is necessary for temporal organization of hippocampal neuronal activity. Nat. Neurosci. *18*, 1123–1132.

Schlesiger, M.I., Boublil, B.L., Hales, J.B., Leutgeb, J.K., and Leutgeb, S. (2018). Hippocampal Global Remapping Can Occur without Input from the Medial Entorhinal Cortex. Cell Rep. *22*, 3152–3159.

Schomburg, E.W., Fernández-Ruiz, A., Mizuseki, K., Berényi, A., Anastassiou, C.A., Koch, C., and Buzsáki, G. (2014). Theta phase segregation of input-specific gamma patterns in entorhinal-hippocampal networks. Neuron *84*, 470–485.

Senzai, Y., Fernandez-Ruiz, A., and Buzsáki, G. (2019). Layer-Specific Physiological Features and Interlaminar Interactions in the Primary Visual Cortex of the Mouse. Neuron *101*, 500–513.e5.

Sharif, F., Tayebi, B., Buzsáki, G., Royer, S., and Fernandez-Ruiz, A. (2021). Subcircuits of Deep and Superficial CA1 Place Cells Support Efficient Spatial Coding across Heterogeneous Environments. Neuron *109*, 363–376.e6.

Skaggs, W.E., and McNaughton, B.L. (1992). Computational approaches to hippocampal function. Curr. Opin. Neurobiol. *2*, 209–211.

Solstad, T., Moser, E.I., and Einevoll, G.T. (2006). From grid cells to place cells: a mathematical model. Hippocampus *16*, 1026–1031.

Stark, E., Roux, L., Eichler, R., and Buzsáki, G. (2015). Local generation of multineuronal spike sequences in the hippocampal CA1 region. Proc. Natl. Acad. Sci. USA *112*, 10521–10526.

Steffenach, H.A., Witter, M., Moser, M.B., and Moser, E.I. (2005). Spatial memory in the rat requires the dorsolateral band of the entorhinal cortex. Neuron *45*, 301–313.

Tingley, D., and Buzsáki, G. (2020). Routing of Hippocampal Ripples to Subcortical Structures via the Lateral Septum. Neuron *105*, 138–149.e5.

Valero, M., Cid, E., Averkin, R.G., Aguilar, J., Sanchez-Aguilera, A., Viney, T.J., Gomez-Dominguez, D., Bellistri, E., and de la Prida, L.M. (2015). Determinants of different deep and superficial CA1 pyramidal cell dynamics during sharp-wave ripples. Nat. Neurosci. *18*, 1281–1290.

Valero, M., Averkin, R.G., Fernandez-Lamo, I., Aguilar, J., Lopez-Pigozzi, D., Brotons-Mas, J.R., Cid, E., Tamas, G., and Menendez de la Prida, L. (2017). Mechanisms for Selective Single-Cell Reactivation during Offline Sharp-Wave Ripples and Their Distortion by Fast Ripples. Neuron *94*, 1234–1247.e7.

Valero, M., Viney, T.J., Machold, R., Mederos, S., Zutshi, I., Schuman, B., Senzai, Y., Rudy, B., and Buzsáki, G. (2021). Sleep down state-active ID2/Nkx2.1 interneurons in the neocortex. Nat. Neurosci. *24*, 401–411.

van de Ven, G.M., Trouche, S., McNamara, C.G., Allen, K., and Dupret, D. (2016). Hippocampal Offline Reactivation Consolidates Recently Formed Cell Assembly Patterns during Sharp Wave-Ripples. Neuron *92*, 968–974.

van Groen, T., Miettinen, P., and Kadish, I. (2003). The entorhinal cortex of the mouse: organization of the projection to the hippocampal formation. Hippocampus *13*, 133–149.

van Strien, N.M., Cappaert, N.L.M., and Witter, M.P. (2009). The anatomy of memory: an interactive overview of the parahippocampal-hippocampal network. Nat. Rev. Neurosci. *10*, 272–282.

Vöröslakos, M., Petersen, P.C., Vöröslakos, B., and Buzsáki, G. (2021). Metal microdrive and head cap system for silicon probe recovery in freely moving rodent. eLife *10*, e65859.

Winson, J. (1978). Loss of hippocampal theta rhythm results in spatial memory deficit in the rat. Science *201*, 160–163.

Witter, M.P. (2007). Intrinsic and extrinsic wiring of CA3: indications for connectional heterogeneity. Learn. Mem. *14*, 705–713.

Witter, M.P., and Amaral, D.G. (1991). Entorhinal cortex of the monkey: V. Projections to the dentate gyrus, hippocampus, and subicular complex. J. Comp. Neurol. *307*, 437–459.

Ye, J., Witter, M.P., Moser, M.B., and Moser, E.I. (2018). Entorhinal fast-spiking speed cells project to the hippocampus. Proc. Natl. Acad. Sci. USA *115*, E1627–E1636.

Zhang, S.J., Ye, J., Couey, J.J., Witter, M., Moser, E.I., and Moser, M.B. (2013). Functional connectivity of the entorhinal-hippocampal space circuit. Philos. Trans. R. Soc. Lond. B Biol. Sci. *369*, 20120516.

Zhang, Y., Cao, L., Varga, V., Jing, M., Karadas, M., Li, Y., and Buzsáki, G. (2021). Cholinergic suppression of hippocampal sharp-wave ripples impairs working memory. Proc. Natl. Acad. Sci. USA *118*, e2016432118.

Please cite this article in press as: Zutshi et al., Extrinsic control and intrinsic computation in the hippocampal CA1 circuit, Neuron (2021), https://doi.org/10.1016/j.neuron.2021.11.015

STAR★METHODS

KEY RESOURCES TABLE

REAGENT or RESOURCE	SOURCE	IDENTIFIER
Bacterial and virus strains		
AAV5-mDlx-ChR2-mCherry	Plasmid gift from Dr. Gord Fishell, Virus custom prepared by Addgene	N/A
AAV1-CamKIIα-stGtACR2-FusionRed	Mahn et al., 2018	RRID:Addgene_105669
AAV5-Syn-DIO-PSAM4-GlyR-IRES-GFP	Magnus et al., 2019	RRID:Addgene_119741
Chemicals, peptides, and recombinant proteins		
μPSEM792 hydrochloride	Tocris	Cat#6865
C&B Metabond	Parkell	Cat#S380
Experimental models: Organisms/strains		
Mouse: B6.Tg(Grik4-cre)G32-4Stl/J	Jackson Laboratories	RRID: IMSR_JAX:006474
Software and algorithms		
KiloSort (template based spike sorting MATLAB software)	Pachitariu M & Cortex-lab	https://github.com/cortex-lab/KiloSort
KilosortWrapper	Peter C. Petersen & Brendon Watson	https://github.com/petersenpeter/KilosortWrapper
Phy (Python GUI for manual spike curation)	Cyrille Rossant, Ken Harris et al.	https://github.com/cortex-lab/phy
Phy plugins	Peter C. Petersen	https://github.com/petersenpeter/phy1-plugins
CellExplorer (Cell classification pipeline and graphical interface)	Petersen et al., 2020	https://linkinghub.elsevier.com/retrieve/pii/S0896627321006565.
MATLAB	MathWorks	https://www.mathworks.com/
Buzcode (MATLAB analysis tools)	Buzsáki Lab	https://github.com/buzsakilab/buzcode (https://doi.org/10.5281/zenodo.5668715)
Custom MATLAB scripts	Ipshita Zutshi	https://github.com/IpshitaZutshi/Zutshi_Neuron2021 (https://doi.org/10.5281/zenodo.5668669)
FMA Toolbox (MATLAB toolbox for Freely Moving Animal (FMA))	Michael Zugaro	https://fmatoolbox.sourceforge.net/
Chronux toolbox	Mitra lab	http://chronux.org/
Other		
Silicon probes	Neuronexus, Cambridge Neurotech, Diagnostic Biochips	A5x12-16-Buz-Lin, H2, H3, P128-2
RHD2000 USB Interface Board	Intan Technologies	C3100
64 channel digital amplifies	Intan Technologies	C3314
PulsePal v2	Sanworks	N/A
3D printed microdrives	Mihály Vöröslakos & Gyorgy Buzsáki	Vöröslakos et al., 2021

RESOURCE AVAILABILITY

Lead contact

Further information and requests for resources and reagents should be directed to and will be fulfilled by the lead contact, György Buzsáki (gyorgy.buzsaki@nyumc.org)

Materials availability

This study did not generate new unique reagents.

Data and code availability

- All the data of this study is publicly available in the Buzsáki Lab Databank: https://buzsakilab.com/wp/public-data/.

Please cite this article in press as: Zutshi et al., Extrinsic control and intrinsic computation in the hippocampal CA1 circuit, Neuron (2021), https://doi.org/10.1016/j.neuron.2021.11.015

- All custom code for preprocessing the data is freely available on the Buzsáki Laboratory repository: https://github.com/buzsakilab/buzcode (Zenodo: 5668715; https://doi.org/10.5281/zenodo.5668715) and scripts specific for analyzing this dataset can be found on https://github.com/IpshitaZutshi/Zutshi_Neuron2021 (Zenodo: 5668669; https://doi.org/10.5281/zenodo.5668669).
- Any additional information required to reanalyze the data reported in this paper is available from the Lead Contact upon request.

EXPERIMENTAL MODEL AND SUBJECT DETAILS

All experiments were approved by the Institutional Animal Care and Use Committee at New York University Langone Medical Center. Mice were kept in the vivarium on a 12-hour light/ dark cycle and were housed 2-3 per cage before surgery. Following surgery, the mice were moved to a 12-hour reverse light cycle (lights on/off at 7 pm/am) and housed individually. Prior to behavior training, mice were provided food and water *ad libitum*, but were water restricted to maintain 85% of their weight during and after behavioral training. We used heterozygous male C57BL/6 transgenic mice (n = 21 mice, Tg(Grik4-cre)G32-4Stl/J, Jax Stock No. 006474), weighing 22-39 g, and aged between 4-12 months old.

METHOD DETAILS

Subjects and surgical procedures

Of the 21 mice used in this study, 6 mice were unilaterally (right hemisphere) injected with AAV5-mDlx-ChR2-mCherry (titer, 1.4x10^{13}, custom prepared from Addgene, plasmids were a gift from Dr. Gord Fishell, (Fernández-Ruiz et al., 2021)) in the mEC, 3 mice were bilaterally injected with AAV5-mDlx-ChR2-mCherry in the mEC, 6 mice were injected with AAV5-mDlx-ChR2-mCherry in the mEC right hemisphere along with AAV1-CamKIIα-stGtACR2-FusionRed in the right dorsal CA1 (titer:1.3x10^{11}, gift from Ofer Yizhar, Addgene viral prep #105669-AAV1; http://addgene.org/105669; RRID:Addgene_105669), and 6 mice were injected with AAV5-Dlx-ChR2-mCherry in the mEC right hemisphere along with AAV5-Syn-DIO-PSAM4-GlyR-IRES-GFP (titer: 2x10^{12}, gift from Scott Sternson, Addgene viral prep #119741-AAV5; http://addgene.org/119741; RRID:Addgene_119741) in bilateral CA3. For the CA3 silencing cohort of mice, mice were given an i.p. injection of either 0.9% saline (Lifeshield Diluent NaCl), or 1.5-3 mg/kg μPSEM792 hydrochloride (Tocris, #6865) diluted in 0.9% saline (working concentration 1 mg/ml, volume injected: 0.04-0.06 ml).

For viral vector injections, mice were anesthetized with isoflurane (1.5%–2.5% in O_2) and mounted in a stereotaxic frame (David Kopf Instruments). Craniotomies were made over the injection sites, and a glass pipette containing virus was slowly lowered into the brain. The following coordinates and viral volumes were used – (a) mEC: 0.2 mm AP from the transverse sinus, ± 3.75 mm from lambda, 150 nL injections each at −1.7mm DV,-1.3mm DV and −0.9 mm DV from the surface of the brain, angled at 6° toward anterior, (b) CA1: 2 injection sites at −1.6mm AP, +1.2mm ML, −1.1mm DV from bregma, and −2.0mm AP, +1.8mm ML, −1.2mm DV from the bregma, 250nl at each site, (c) CA3: 6 injection sites at −1.7mm AP, ± 1.9mm ML, −2.0mm DV, −2.3mm AP, ± 2.5mm ML, −2.2mm DV, and −2.8mm AP, ± 3.0mm ML, −3.2mm DV from bregma, 250nl, 350nl and 500nl at each site respectively. After each injection, the pipette was left in place for atleast 10-15 minutes. The injections were administered at a flow rate between 25-50 nl/min using a microsyringe pump (World Precision Instruments, UMP3 UltraMicroPump). The constructs were allowed to express for at least 2-3 weeks before the mice were implanted with silicon probes. Following surgery, an opioid analgesic was injected (Buprenex at 0.06 mg/kg, 0.015 mg/ml, IM).

Animals were implanted with 64 or 128 channel silicon probes into CA1 (6 mice were implanted with Neuronexus A5x12-16-Buz-Lin-5mm-100-200-160-177 probes, 9 mice were implanted with Cambridge NeuroTech H2 probes, 4 mice were implanted with Cambridge NeuroTech H3 probes, 2 mice were implanted with Diagnostic Biochips ASSY-INT128, P128-2 probes). The coordinates used for CA1 implants was either −1.8mm AP, +1.5 mm ML from bregma, or −2.0 AP, +1.7mm ML from bregma. A ground screw coupled with a 0.005'' stainless steel wire (A-M Systems, #792800) was implanted in the skull above the cerebellum, and a grounded copper mesh hat was constructed, shielding the probes. Metabond was used to cement the base to the skull of the animal (C&B Metabond, #S380). The probes were mounted on custom-made 3D-printed micro-drives to allow precise adjustment of vertical position of sites after implantation (Vöröslakos et al., 2021). Local CA1 silencing was achieved by attaching a 100 μm optic fiber glued to a ceramic ferrule (0.22 NA, Thorlabs, FG105LCA and Thorlabs, 30126L9) to the shanks of the silicon probe. mEC silencing was achieved by implanting a 200 μm optic fiber glued to a stainless-steel ferrule (0.50 NA, Thorlabs, FP200URT and Thorlabs, SFLC230) unilaterally or bilaterally over the mEC (+0.2 mm AP from the transverse sinus, ± 3.75 mm from lambda, −0.6 mm DV from the surface of the brain, angled 6° toward anterior). Light was delivered by coupling the optic fiber to a laser diode (450 nm blue, Osram) and stimulation pulses were delivered using an isolated current driver (Thorlabs, LDC205C). Light intensity was calibrated across animals to achieve maximal reduction in theta power with the least power and was between (2 mW to 8 mW for the mEC optic fiber, and 0.5mW to 1.5 mW for the CA1 optic fiber). Light output was measured using a power meter (Thorlabs, PM100D).

Viral expression and the position of the probe was confirmed at the end of each experiment. The mice were perfused with cold saline solution (0.9%) followed by pre-made 4% paraformaldehyde (PFA) in in phosphate-buffered saline (PBS) solution (Affymetrix USB). Brains were post-fixed for 24h in 4% PFA and sectioned coronally and sagitally to visualize both the hippocampus (coronal)

Please cite this article in press as: Zutshi et al., Extrinsic control and intrinsic computation in the hippocampal CA1 circuit, Neuron (2021), https://doi.org/10.1016/j.neuron.2021.11.015

and mEC (sagittal). Sections were obtained with 40-50 μm thickness using a vibrating blade microtome (Leica, VT1000S), mounted on electrostatic slides, coverslipped with DAPI Fluoromount-G (Southern Biotech, 0100-20), and imaged using a virtual slide microscope (Olympus, VS120). No additional immunohistochemistry or tissue processing was done to visualize viral fluorescence.

Recordings and behavior

Animals ran on the delayed spatial alternation task for 40-60 laps (approximately 40 minutes) and were then recorded from in their home cage for 3-4 hours. Within the homecage, stimulation was provided randomly for up to three different manipulations (individual and combined manipulations) for atleast 30 trials (5 s ON, 25 s OFF for 15 minutes, followed by 15 minutes of no stimulation). Therefore all homecage manipulations lasted for atleast 180 minutes, and the median total time spent in the home cage was approximately 2.5 hours. On most days, the mice subsequently ran a second spatial alternation task session with a different stimulation. For sessions with CA3 silencing, mice were injected with μPSEM792 or saline mid-way through the home cage recording session, and always ran the second behavioral session. Animals were handled daily and accommodated to the experimenter, recording room and cables, and trained to obtain a minimum performance of 80% in the delayed version of the alternation task before the start of experiments (training lasted 7-10 days). The maze was custom-built in the lab with dimensions 70cm x 40 cm (1 m above the floor) and 3.7 mm high walls (McMaster-Carr, PVC U-Channel #85065K55). Water was delivered by solenoids (Cole-Parmer, EW-98302) and activated by the animal crossing infrared beams (NOYITO E180D80NK) at the reward and delay zones. Maze doors, water delivery, and optogenetic stimuli were controlled by a custom-made Arduino-based circuit (Valero et al., 2015).

Electrophysiological data were acquired using an Intan RHD2000 system (Intan Technologies) digitized at 30-kHz. The wideband signal was downsampled to 1250 Hz and used the LFP. A pulley system was designed to counteract the weight of the tether and headstage. In the home cage, optogenetic stimulation was delivered as 5 s-long square pulses, repeated every 30 s for 30-50 trials, using PulsePal2 (Sanworks, v2) connected with MATLAB. On the maze, stimulation was triggered by TTLs from the IR sensors, using PulsePal2. The animal’s position was monitored using a Basler camera (acA1300-60 gmNIR, Graftek Imaging) sampling at 30Hz to detect a head-mounted red LED. Position was synchronized with neural data with TTLs signaling shutter position.

Unit clustering and neuron classification

Spikes were extracted and classified using Kilosort (Pachitariu et al., 2016) using a custom pipeline KilosortWrapper (https://github.com/brendonw1/KilosortWrapper). Automated sorting was followed by manual curation of the waveform clusters using Phy (https://github.com/cortex-lab/phy) and custom plugins for Phy (https://github.com/petersenpeter/phy1-plugins). Kilosort clustering was performed with the following parameters: ops.Nfilt:6*numberChannels, ops.nt0:64;ops.whitening:’full’;ops.nSkipCov:1;ops.whiteningRange:64;ops.criterionNoiseChannels:0.00001 ; ops.Nrank: 3; ops.nfullpasses: 6; ops.maxFR: 20000; ops.fshigh: 300; ops.ntbuff: 64; ops.scaleproc: 200; ops.Th: [4 10 10]; ops.lam: [5 20 20]; ops.nannealpasses: 4; ops.momentum: 1./[20 800]; ops.shuffle_clusters: 1. Units were separated into putative pyramidal cells and narrow waveform interneurons using their autocorrelograms, waveform characteristics and firing rate. This classification was performed using CellExplorer (Petersen et al., 2020). Units were defined as CA1 or CA3/DG cells based on their recording position on the silicon probe and after confirming the location of the probe with histology.

Ripple detection

Ripples were detected as described previously (Tingley and Buzsáki, 2020), and the code is available at the Buzsáki lab github repository (bz_FindRipples). Briefly, the raw LFP (1250 Hz) was filtered (130-200 Hz; Butterworth; order = 3) and was transformed to a normalized squared signal (NSS). This signal was used to identify peaks that were beyond 5 standard deviations above the mean NSS. The beginning/end cutoff of the ripple was defined by a threshold of 2 standard deviations above the mean NSS. Ripple duration limits were between 20ms and 100ms. In addition, estimated EMG from the LFP (Schomburg et al., 2014) was used to exclude EMG related artifact. The peak of the ripple (max power value > 5 standard deviations) was defined as time 0 for the ripple. Ripples were defined across the entire duration of a day, including both periods in the maze and the homecage.

CSD and coherence analysis

The second spatial derivative of the LFP profile was used to calculate the CSD (Makarov et al., 2010; Mitzdorf, 1985). The CSD power spectra was calculated using a custom written script (bz_PowerSpectrumSlope), which calculates the FFT using the MATLAB function ‘spectrogram’ (window size, 1 s; dt, 0.1 s). Theta CSD magnitude was calculated using the script bz_eventThetaCSD2. First, periods of LFP while the mouse was running on the central arm of maze (either baseline or stimulation) were extracted. This LFP from oriens was filtered (6-12 Hz; Butterworth; order = 3) and the instantaneous phase was estimated using a Hilbert transform. Theta peaks greater than 2 standard deviations from the LFP squared signal were determined. Segments of the LFP signal on each channel along the depth of the shank were subsequently aligned with reference to the peak, and the differential between successive average aligned channels was used to generate the CSD magnitude. Unless mentioned otherwise, all analysis was restricted to the central arm of the Figure 8 maze.

LFP coherence was measured using the script bz_lfpCoherence. The coherogram was calculated using a multi-taper estimation using the chronux function ‘cohgramc’ (window, 2 s; overlap,1 s; step, 1;padding, 0), and the magnitude and phase of the resultant coherogram was examined. Unless mentioned otherwise, all analysis was restricted to the central arm of the Figure 8 maze.

Please cite this article in press as: Zutshi et al., Extrinsic control and intrinsic computation in the hippocampal CA1 circuit, Neuron (2021), https://doi.org/10.1016/j.neuron.2021.11.015

Theta phase locking, phase precession, and oscillation frequency analysis

LFP from oriens was filtered and the instaneous phase was determined using a Hilbert transform. Theta phase locking was determined by calculating the phase angles for each timestamp where an action potential occurred, restricted to the defined central arm of the figure-8 maze (bz_PhaseModulation). A histogram of phase angles was calculated, and the circular mean and resultant vector (Berens, 2009) were calculated for each neuron. Only neurons that were significantly modulated (Rayleigh test) were included in the analysis. Phase locking was estimated separately for no stimulation and stimulation trails.

To measure phase precession, theta phase was first estimated as described above. Next, place fields were normalized between 0 and 1 to the beginning to end of the field. A circular-linear regression was generated for spikes occurring within the bounds of the fields, and the slope and significance of the regression line is reported. Significance was achieved by a $p < 0.05$. Boundaries of ± 1.5 cycles were used to constrain the circular-linear regression.

Assembly analysis

Cell assemblies were defined using an unsupervised statistical framework based on a hybrid PCA followed by ICA (Lopes-dos-Santos et al., 2013; van de Ven et al., 2016). Spike trains of each neuron were binned in 25-ms intervals by concatenating spikes only in the central arm of the maze and z-scored rates were calculated for each bin. Assemblies were defined in two ways – first by combining baseline and stimulation trials, but also by examining baseline and stimulation trials independently. To define assemblies, spike trains from periods of interest were convolved with a Gaussian kernel (SD = 10 ms), and the matrix of firing correlation coefficients for all pairs of neurons was constructed. Principal components with eigenvalues that exceeded the threshold for random firing correlations (using the Marčenko-Pastur law) were used to determine the number of assemblies. Next, using the fast-ICA algorithm (Ritchey et al., 2015), we determined the vector of weights (contribution of each neuron) for each assembly (component). High contributing neurons were defined as cells that had weights > 2 standard deviations from the mean weight of all neurons. The strength of each assembly's activation as a function of time was determined by multiplying the convolved z-scored firing rate of a given neuron at a given time by the weight of that neuron's contribution to the assembly. The product of these weighted spike counts was then summed for all nonidentical pairs of neurons to generate the instantaneous activation strength. For each assembly, irrespective of which period it was defined in, the average activation strength during baseline, and stimulation conditions was subsequently compared, and a measure of change in activation strength (Δ assembly activity) was defined as -

(Stim-baseline)/(stim+baseline). For within baseline, and within stimulation stability measures, Δ assembly activity was calculated by dividing baseline or stimulation trials into half and calculating Δ assembly activity between the two halves.

The fraction of assemblies increasing or decreasing in expression during each manipulation was defined by calculating a threshold of mean ± 2*std. dev of the stability during baseline sessions, and measuring the fraction of assemblies whose expression changed greater than, or less than this threshold during stimulation (Figure 5E).

We also implemented a cell-by-cell correlation analysis to quantify pairs of co-active cells. As described above, spike train matrices for spikes within the center arm were generated, but in this case by using 125 ms (theta timescale) bins. Periods of either baseline or stimulation trials were extracted, and further divided into halves. Subsequently, the spike trains between all cell pair combinations were correlated (Spearman correlation) with each other for each baseline or stimulation half. Cell pair correlation values were clustered into groups of co-firing neurons (MATLAB function *linkage*, followed by *cluster,* 'maxCluster',5) for the first half of each session type, and the same order was maintained for the second half. Cell pair correlation matrices were next generated by sorting according to clustered neurons for baseline and stimulation sessions separately, and the stability of cell pair correlations was measured by correlating between the two half session matrices for baseline and stimulation separately. Changes in co-firing pairs between baseline and stimulation was measured by sorting cell-pair correlation values during stimulation by cell clusters defined during baseline, and correlating between the baseline versus re-sorted stimulation matrix (Figures S5K and S5L). Because the correlation matrix is symmetric around the diagonal, only the bottom half of each matrix was correlated to each other (excluding the diagonal, which is equal to 1). Only sessions with atleast 5 active CA1 pyramidal cells were included in these analyses.

Place field analysis

Rate maps were generated by first binning spiking data into 1.75 cm wide-bins, generating maps of spike counts and occupancy for periods when the animal's speed was > 1 cm/s. Maps for left and right bound trials, and stimulation and non-stimulation trials were generated separately. A smoothed rate map (smoothing size: 2 bins) was constructed by dividing the spike map by the occupancy map. Place fields were defined from these rate maps by finding peaks in the rate map. The field boundaries were defined till the rate was above 20% of the peak firing rate. Place fields cleared all criteria if they were between 8.75 cm and 75 cm wide, had a minimum peak firing rate of 2 Hz. Additional fields were defined if they cleared the above-described criterion. Spatial rate-map correlations for individual cells between trials was calculated as the average pixel-by pixel Spearman correlation of the smoothed-averaged firing rate maps. PV correlations were defined by stacking the rate maps of all cells in the same order and calculating the bin-by-bin Spearman correlation across all cells for a single bin. Baseline PV correlations were calculated by dividing baseline sessions into halves and measuring the PV correlation of each half against each other. Rate map stability was defined by generating rate maps for the first and second halves of each trial type (e.g., no stim, left trials), and correlating these half-session rate maps. Because the within baseline comparison was on session halves, i.e., fewer trials to generate the ratemap, the baseline versus stimulation comparisons were also performed on correlations between the first half of baseline, and first half of stimulation trials.

Please cite this article in press as: Zutshi et al., Extrinsic control and intrinsic computation in the hippocampal CA1 circuit, Neuron (2021), https://doi.org/10.1016/j.neuron.2021.11.015

Spatial information was calculated in bits per spike (Skaggs and McNaughton, 1992) as,

$$\mathrm{SPI} = \sum_i p_i \frac{\lambda_i}{\lambda} \log 2 \frac{\lambda_i}{\lambda}$$

where λ_i is the mean firing rate of a unit in the ith bin, λ is the overall mean firing rate, and p_i is the probability of the animal being in the i_{th} bin (ocuupancy in i_{th} bin/total time).

Downsampled maps were generated by first detecting the number of spikes in the center versus side arms for each cell separately for baseline and stimulation trials. Spikes in the baseline trials were randomly subsampled to match the number of spikes during stimulation, separately for the center and side arms of the maze. Rate maps were constructed using these downsampled spike matrices, and all subsequent analyses were conducted as described above.

QUANTIFICATION AND STATISTICAL ANALYSIS

Statistical analysis

Data collection was not performed blinded to the subject conditions, but data analysis or behavior experiments did not require manual scoring. All stimulation conditions were performed randomly, and animals from different experiments were run in parallel cohorts. No specific analysis was used to estimate minimal population sample, but the number of animals, trials and recorded cells were larger than or similar to those employed in previous studies (McKenzie et al., 2021; Senzai et al., 2019; Valero et al., 2021; Zhang et al., 2021). All statistical tests were conducted using MATLAB R2021a, and the details of the tests used are described with the results. Unless otherwise noted, all tests used non-parametric comparisons of means and variance (Wilcoxon paired signed rank tests, Wilcoxon rank-sum test, Kruskal-Wallis one-way analysis of variance, and Friedman tests). When parametric tests were used, the data satisfied the criteria for normality (Kolmogorov-Smirnov test) and equality of variance (Bartlett test for equal variance). All posthoc tests were performed using Tukey honest significant differences and correcting for multiple comparisons. Boxplots represent the median and 25th and 75th percentiles, and the whiskers represent the data range. In boxplots without datapoints, outliers were excluded from the plots, but always included in the statistical analysis.